Low Profile Corrugated Structures for Surface Wave Suppression and Multipath Mitigation in GNSS Antennas

by

Ehsan Taghdisi

A thesis submitted in partial fulfillment of the requirements for the degree of

Master of Science

in

Engineering Management

Department of Mechanical Engineering

University of Alberta

Abstract

Multipath interference is an error generating issue in high-accuracy global navigation satellite system (GNSS) applications. Since the propagation of surface waves along the surface of antenna structure is the root cause for reception of multipath signals in GNSS antennas, surface wave suppressing ground structures are needed for GNSS antennas that are employed in high-precision GNSS applications. Two-dimensional (2D) corrugated structures, also known as choke rings, are commonly used as the ground structure for high-accuracy GNSS antennas. Despite their superior performance, choke rings suffer from large size, heaviness, costly fabrication, and inability to integrate with printed circuit board (PCB) structures. The objective of this thesis has been to design low-profile substitutions for these bulky structures.

First, a review of literature is conducted on the multipath signals, surface waves, and surface wave suppressing ground structures to acquire a deep understanding of the problem and techniques to analyse it.

Then, a compact dual-band substrate integrated choke ring (SICR) ground structure has been designed by engineering the location of via holes and partial copper cladding of the substrates in a multilayer structure.

Next, a novel technique for miniaturization of corrugated structures is presented and folded corrugations are introduced. The miniaturization is achieved by implementing a fold or slit inside each corrugation. The proposed miniaturization technique is modeled using the modal expansion method and an equivalent circuit is extracted which precisely models the surface impedance

of the proposed folded corrugation. A time-efficient deign procedure is presented based on the equivalent circuit model and a Folded SICR (FSICR) structure is designed.

Finally, the idea of folded corrugations is expanded to multi-folded corrugations (MFCs) to achieve further miniaturization. The design procedure is adjusted as well to design dual-band multi-folded corrugated structures. A dual-band Double-Folded SICR (DFSICR) structure is designed to suppress the propagation of surface waves over the main GNSS frequency bands, L1 (1573-1587 MHz) and L2 (1215-1240 MHz).

The performance of the proposed structures has been investigated by mounting a right-handed circularly polarized (RHCP) GNSS antenna on it. The introduced designs demonstrate significant multipath mitigation capabilities, close to that of a classic choke ring, while they eliminate the drawbacks of a conventional one. An example design of DFSICR shows miniaturization of 85% in height and 38% in diameter compared to the conventional choke rings. It also demonstrates weight reduction of more than 90%, thanks to its substrate integrated design.

It worth noting that although the motivation behind the introduced miniaturization technique has been to address a problem in GNSS antennas, the approach looks promising for miniaturization of other corrugated structures such as spoof surface plasmon polartion (SPP) waveguides and components.

Preface

This thesis is an original work by Ehsan Taghdisi as the main contributor. I have been responsible for conducting the research, analysis, design, simulations, test, and manuscript writing. In all of the co-authored publications, the contribution of co-authors, Dr. Saeid Ghaffarian, Dr. Rashid Mirzavand, and Dr. Pedram Mousavi, has been mainly advisory and editorial. Dr. Ghaffarian has helped with the test and measurements of the fabricated designs as well.

Section 4.1 with slight modifications has been published as E. Taghdisi, S. Ghaffarian, R. Mirzavand and P. Mousavi, "Compact Substrate Integrated Choke Ring Ground Structure for High-Precision GNSS Applications," 2020 IEEE International Symposium on Antennas and Propagation and North American Radio Science Meeting, 2020, pp. 1705-1706.

Parts of the chapter 3 in combination with section 4.3 are accepted to be published as E. Taghdisi, S. Ghaffarian, and R. Mirzavand, "Low-Profile Substrate Integrated Choke Rings for GNSS Multipath Mitigation," IEEE Transactions on Antennas and Propagation.

Section 4.2 in combination with parts of chapter 3 are intended for publication with Dr. Ghaffarian and Dr. Mirzavand as co-authors.

To the Victims of Flight PS752

Acknowledgements

I would like to thank Dr. Rashid Mirzavand for his advice during this research project and Dr. John Doucette for supporting the Intelligent Wireless Technology group after the tragic loss of Dr. Pedram Mousavi in the PS752 air disaster.

I also would like to thank the examiners of my thesis, Dr. Ashwin Iyer, and Dr. Kambiz Moez for their constructive feedback.

The financial support of this work from the National Science and Engineering Research Council of Canada, the Alberta Innovates, and the NovAtel Inc. is also greatly appreciated.

Contents

1 Introduction **1**

2 Background and Review of Literature **4**
2.1 Multipath Signals and Multipath Resistant Radiation Patterns 4
2.2 Surface Waves 5
2.3 Surface Wave Suppressing Structures 6
2.3.1 Artificial Magnetic Conductors (AMCs) 7
2.3.2 Soft Surfaces 8
2.3.3 Electromagnetic Band-Gap Structures (EBGs) 9
2.3.4 High-Impedance Surfaces (HISs) 10
2.4 Choke Rings and their Applications 13

3 Proposed Miniaturization Technique and the Introduction of Folded and Multi-Folded Corrugations **15**
3.1 Analysis of Folded Corrugations using Modal Expansion Technique 16
3.2 Demonstration of Miniaturization Capability of Folded Corrugations 21
3.3 Parametric Analysis of Folded Corrugations 22
3.4 Multi-Folded Corrugations and their Equivalent Circuit 22
3.5 Design of Dual-Band Multi-Folded Corrugated Structures . . . 25

4 Designed Choke Ring Structures, Results, and Discussion **29**
4.1 Dual-Band Substrate Integrated Choke Rings 30
4.2 Single-Band Folded SICR (FSICR) 32
4.3 Dual-Band Double-Folded SICR (DFSICR) 35
4.3.1 Gain and AR 35
4.3.2 Bandwidth Analysis 38
4.3.3 Visualization of the Dual-Band Behavior 38
4.3.4 Study of Slit Parameters 40
4.3.5 Phase Center Stability Analysis 43
4.3.6 Prototyping 44
4.3.7 Measurement Results 45
4.3.8 Comparison with Other Multipath Mitigating Ground Structures 46

5 Conclusion and Future Directions **50**
5.1 Overall Contributions 50
5.2 Future Directions 51

References **52**

List of Tables

2.1 Specifications of a Multipath Resistant GNSS Antenna 5

4.1 Phase center of the antenna in presence and absence of the DFSICR. 43
4.2 Comparison between the proposed DFSICR and other multipath mitigating ground structures 49

List of Figures

2.1 Illustration of multipath phenomenon. 5
2.2 Illustration of the fields of TE and TM surface waves on a grounded dielectric slab. 6
2.3 A corrugated surface, and example of an AMC when $s+t << \lambda$ and $d = \lambda/4$ (a) Top view (b) Front view. 8
2.4 A choke ring structure, and example of a soft surface when $s + t << \lambda$ and $d = \lambda/4$ (a) Isometric view (b) Cross section. . 9
2.5 An EBG structure (a) Top view (b) Front view. 10
2.6 Illustration of capacitance and inductance in the unit cell of the mushroom-like EBG. 10
2.7 Propagation of surface waves over a general impedance surface. 11

3.1 Cross section of a folded corrugation (unit cell of a folded corrugated structure). 16
3.2 Equivalent circuit of the folded corrugated structure 20
3.3 Comparison between the normalized surface impedance of a non-folded corrugation and a folded one for $d_1 = d_2 = 9.2$ mm, $\epsilon_r = 4.7$, $C_{\text{eq}} = 0.35$ pF. 21
3.4 Value and variation of C_{eq} for different values of slit width and corrugation width assuming $\epsilon_r = 4.7$, $d_1 = d_2 = 9.2$ mm. . . . 22
3.5 A multi-folded corrugation. 23
3.6 Relative error of estimating slit capacitance using ((3.34)). . . 24
3.7 Equivalent circuit of a double-folded corrugation. 24
3.8 (a) Unit cell of a dual-band corrugated structure (b) Normalized surface impedance of the unit cell for $g_1 = 14$ mm, $g_2 = 19$ mm, $w_1{}' = w_2{}' = 9.4$ mm, $w_3{}' = 18$ mm, $t = 2$ mm, $d_1 = d_2 = 7.5$ mm, $\epsilon_r = 4.7$. 28

4.1 A conventional choke ring structure (a) Isometric view (b) Cross section and typical dimensions, $a = 342$ mm, $d = 66$ mm, $S = 19$ mm, $t = 6$ mm. 29
4.2 (a) Cross section of the SICR (b) Design parameters of the SICR ground structure. $a = 204$ mm, $s_1 = 10$ mm, $s_2 = 16$ mm, $s_3 = 7$ mm, $t = 2$ mm, $t_2 = 4$ mm, $d_1 = d_2 = 7.6$ mm, $d_3 = 3.81$ mm, $\epsilon_r = 9.8$ 30
4.3 Comparison of the radiation patterns of the VEXXIS 502 mounted on the SICR, conventional choke ring, and by itself at (a) 1575 MHz (b) 1227 MHz. 31
4.4 Comparison of the ARs of the VEXXIS 502 mounted on the SICR, conventional choke ring, and by itself. 32

4.5 Single-band FSICR (a) Expanded view (b) Cross section and design parameters. $a = 178$ mm, $r = 63.5$ mm, $s = 10$ mm, $w = 5$ mm, $t = 3$ mm, $t_2 = 5$ mm, $d = 6.35$ mm, thickness of conductors= 0.018 mm, $\epsilon_r = 9.8$. 33
4.6 Comparison between gains of the antenna when it is mounted on the FSICR, classic choke ring, and by itself at 1575 MHz. 34
4.7 Comparison between ARs of the antenna when it is mounted on the FSICR, classic choke ring, and by itself at 1575 MHz. 34
4.8 Variation of the gain of the antenna mounted on the DFSICR over Upper GNSS frequency band (L1 and G1). 35
4.9 Dual-band DFSICR (a) Expanded view (b) Cross section view and design parameters . $a = 227$ mm, $r = 63.5$ mm, $g_1 = 14$ mm, $g_2 = 20$ mm, $w_1^{'} = w_2^{'} = 11.5$ mm, $w_3^{'} = 18.3$ mm, $t = 2$ mm, $t_2 = 4$ mm, $d = 3.2$ mm, thickness of conductors= 0.018 mm, $\epsilon_r = 4.7$. 36
4.10 Comparison between gains of the antenna when it is mounted on the DFSICR, classic choke ring, and by itself at (a) 1575 MHz (b) 1227 MHz. 37
4.11 Comparison between ARs of the antenna when it is mounted on the DFSICR, classic choke ring, and by itself at (a) 1575 MHz (b) 1227 MHz. 37
4.12 Variation of the gain of the antenna mounted on the DFSICR over (a) Upper GNSS frequency band (L1 and G1) (b) L2 frequency band. 39
4.13 Magnitude of electric field over the surface of the dual-band DFSICR at (a) 1575 MHz (b) 1227 MHz. 40
4.14 Variation of the AR of the antenna mounted on the DFSICR for (a) $w_1^{'}$, 1575 MHz (b) $w_3^{'}$, 1227 MHz (c) g_1, 1575 MHz (d) g_2, 1227 MHz. 42
4.15 Top view of the (a) Top laminate (b) Middle laminate (c) Bottom laminate (d) Assembled structure. 44
4.16 Measurement setup (a) source antenna (b) antenna under test. . . 46
4.17 Comparison between the simulated and measured gains of the antenna mounted on DFSICR at (a) 1560 MHz (b) 1610 MHz (c) 1215 MHz (d) 1240 MHz. 47
4.18 Measured ARs of the antenna mounted on DFSICR. 48
4.19 Measured S_{11} of the antenna with and without DFSICR. . . . 48

Chapter 1

Introduction

Real-time positioning and navigation using the global navigation satellite system (GNSS) has made cutting-edge and efficient technologies available in every aspect of modern life such as agriculture, surveying, mapping, construction, transportation, automation, and unmanned vehicles [1]. The phenomenon known as multipath is one of the major sources of error in GNSS, which prevents accomplishing centimeter-level accuracy required in many applications [2]. This phenomenon occurs when the satellite signal reflects or diffracts from surrounding objects (e.g., towers and trees on the Earth and spacecraft body in space), and reaches the receiving antenna indirectly; in addition to the line of sight (LOS) signal. The LOS and multipath signals are summed at the receiver input, causing error in satellite-to-user range computation and positioning. Different post-processing techniques are reported in the literature to detect and discard the multipath signals [3]–[6]. Although these techniques have been successful in estimating long-delayed multipath signals and canceling them out, they can hardly distinguish the short-delayed multipath signals with the LOS signal. This is due to the fact that short-delayed multipath signals are created by very nearby obstacles, and hence, do not substantially differ in amplitude and phase with the LOS signal. This problem is more challenging to solve in time-dependent dynamic GNSS applications that rely on real-time or near-real-time positioning, where all processing and computation must be completed over a few seconds.

In contrary to post-processing techniques, a properly designed receiving

antenna can reject the multipath signals in real-time as they usually reach the antenna at near or below horizon angles [7]–[10]. It should be noted that the polarization of right-handed circularly polarized (RHCP) satellite signal, changes to left-handed circularly polarized (LHCP) after reflection. As a result, multipath resistant GNSS antennas with low side and back radiation, and high polarization isolation, which are able to reject multipath signals, are highly in demand in high-precision GNSS applications.

A major limiting factor in realizing such radiation patterns is the propagation of surface waves along the ground plane of the antenna [7]–[9]. When these surface waves reach the edges of the ground plane, they diffract and cause considerable levels of side lobes and back lobes, and consequently, force the antenna to receive more multipath signals.

A variety of approaches has been reported in the literature to mitigate the propagation of surface waves along the ground plane of the antenna and realize multipath-resistant radiation patterns. For instance, planar and non-planar antenna arrays are used to place nulls at the points of interference [11]–[13]. However, antenna arrays often need complex feeding networks, mutual coupling considerations, and are large and costly. Thus, they are mostly used in military applications where intentional interference and jamming signals must be suppressed in addition to multipath interference. In another approach, corrugated structures are employed to decrease side radiations and increase the boresight gain of antennas by manipulating the interaction between surface waves and spatial radiation [14], [15]. A specific type of corrugated structures, called choke rings, are utilized beneath the ground plane of the antenna as the most common commercial solution to the GNSS multipath interference problem [7]. Although choke ring structures are bulky, quite heavy (about 5 kilograms), and costly to fabricate, they are usually employed in GNSS applications that require centimeter-level accuracy due to their superior multipath mitigating characteristics. As an alternative to choke ring ground planes, Electromagnetic Band Gap (EBG) structures are utilized to block side and back radiations by creating a high impedance region around the antenna and preventing the propagation of surface waves [16]–[18]. EBG structures are much

lighter and more cost-effective than choke ring structures since they can be fabricated in multilayered printed circuit board (PCB) technology. Despite this, high periodicity is needed to achieve acceptable multipath rejection, which results in larger area consumption, while the performance is not often as good as the choke rings. Thus, choke rings have remained the dominant antenna ground structures for high-accuracy GNSS systems.

A choke ring may be miniaturized by filling its corrugations with dielectrics; however, dielectric loading decreases the operational bandwidth [8], [9]; and a dual-band design is required to cover the lower GNSS band ($1165 - 1300$ MHz) and upper GNSS band ($1560 - 1610$ MHz), simultaneously. A dual-band dielectric-loaded choke ring has been proposed in [8] lately, which covers the most common GNSS frequency bands, L1 (1563-1587 MHz) and L2 (1215-1240 MHz). Although this design is smaller than the conventional one reported in [7], the metallic nature of corrugations still imposes the heaviness and the inability to integrate with PCB circuits. Additionally, two types of dielectrics or a grooved one must be used to realize the dual-band behavior, which may result in a complicated and costly fabrication process. Therefore, state of the art research is required to develop appropriate substitutions for the choke rings.

The objective of this work is to design low-profile, low-cost, and substrate integrated ground structures for GNSS antennas without sacrificing the antennas multipath rejection performance.

Chapter 2

Background and Review of Literature

2.1 Multipath Signals and Multipath Resistant Radiation Patterns

As discussed in chapter 1, the reception of multipath signals at the GNSS antennas leads to inaccuracies in locating and navigating the user. The goal of this section is to provide a more visual and intuitive explanation of the multipath phenomenon and to illustrate the ideal radiation pattern of a multipath rejecting GNSS antenna.

Fig. 2.1 illustrates an example of multipath phenomenon. Ray 1 depicts the direct satellite signal, also known as line-of-sight (LOS) signal, whereas, ray 2 and 3 depict the reflections of the satellite signal from ground and a nearby object ,respectively. Thus, ray 2 and 3 are multipath signals that approach the antenna from paths other than the direct path. If the receiving antenna demonstrates a considerable gain, compared to the boresight gain, at the reaching angles of the multipath signals, the antenna receives the multipath signals which may lead to significant errors in the receiver.

One may observe that the multipath signals reach the antenna at low or below elevation angles. As a result, to avoid receiving the multipath signals, the ideal GNSS antenna should demonstrate no radiation gain at low or below horizon angles. Since the GNSS systems utilize RHCP polarization, the receiving antenna should be designed for pure RHCP radiation/reception. It is

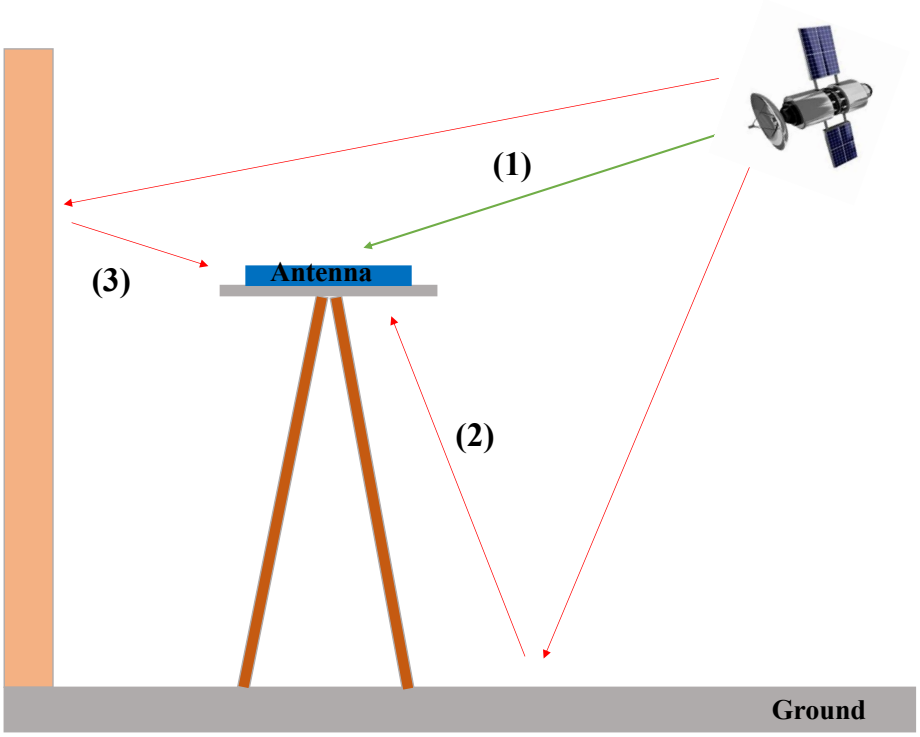

Figure 2.1: Illustration of multipath phenomenon.

Table 2.1: Specifications of a Multipath Resistant GNSS Antenna

Boresight Gain (dBic)	Polarization	3-dB Axial Ratio Beamwidth (degrees)	Front-to-Back (dB)
> 4	RHCP	180	> 15

obvious that the realization of such an ideal radiation pattern may not be possible in practice, however, the criteria listed in Table 2.1 is usually considered as acceptable performance in high-precision GNSS applications.

2.2 Surface Waves

Surface wave (SW) is a specific type of wave which propagates along a surface; e.g. on the surface of a grounded dielectric slab or a corrugated conductor. For instance, on a grounded dielectric slab, SWs are identified by the type of fields that are mostly confined in the dielectric and near the dielectric-air interface, while decaying exponentially outside the dielectric [19]. SWs are mainly di-

vided into two types: transverse electric (TE), and transverse magnetic (TM) as illustrated in Fig. 2.2. The complete analysis and formulation of these waves can be found in classic electromagnetics books such as [19]. Cut-off frequencies of TE and TM surface waves propagating along a grounded dielectric slab are given in [19] as:

$$f_{c_{\mathrm{TE}}} = \frac{(2n-1)c}{4d\sqrt{\epsilon_r - 1}}\ ,\ n = 1, 2, 3, ... \tag{2.1}$$

$$f_{c_{\mathrm{TM}}} = \frac{nc}{2d\sqrt{\epsilon_r - 1}}\ ,\ n = 0, 1, 2, ... \tag{2.2}$$

where c is the speed of light in free space, and d and ϵ_r are the thickness and permittivity of the dielectric, respectively. As one may notice, the cut-off frequency of TM_0 mode is zero. Thus, the TM_0 mode always exists on the dielectric-air interface of planar antennas. These waves diffract when they face a discontinuity, e.g. the edges of the ground plane of the antenna. This diffraction enhances the level of the side lobes and back lobes of the antenna and makes it more susceptible to multipath interference [7], [8].

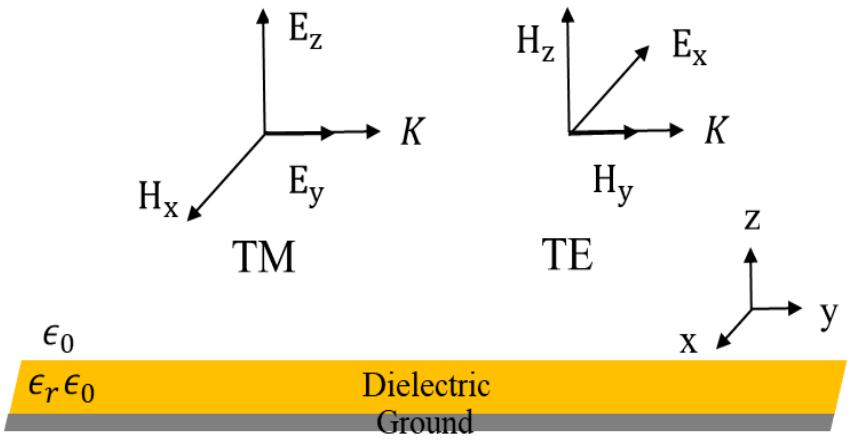

Figure 2.2: Illustration of the fields of TE and TM surface waves on a grounded dielectric slab.

2.3 Surface Wave Suppressing Structures

To avoid the diffraction of SWs at the edges of the ground planes of antennas, and achieve multipath resistant radiation patterns, the propagation of

SWs should be suppressed by using electromagnetic surfaces that effectively change the boundary conditions. Periodic surfaces may be used beneath the antenna structure to change the boundary conditions and force the electric or magnetic fields of surface waves to be zero, preventing their propagation in practice. Such periodic structures have been reported in literature with names such as artificial magnetic conductors (AMCs), soft surfaces, Electromagnetic Band-Gap Structures (EBGs), and high-impedance surfaces (HISs). Although these structures have been initially developed from different perspectives, their principles of operation are closely related [20]. Here, we provide a brief description of these surfaces.

2.3.1 Artificial Magnetic Conductors (AMCs)

An AMC is a textured surface that mimics the characteristics of perfect magnetic conductor (PMC), i.e., zero tangential magnetic field and zero reflection phase, over a limited frequency band. An AMC does not allow the propagation of TM surface waves on its surface by imposing the zero tangential magnetic field boundary condition on the surface. As a result of this boundary condition, the surface impedance, defined as the ratio of electric field to magnetic field on the surface, is high [21]. Thus, an AMC is sometimes called as a HIS.

An example of an AMC surface is a the surface of a corrugated metal if the corrugation width and depth are subwavelength and quarter wavelength, respectively, as depicted in Fig. 2.3. This is because each narrow corrugation can be modeled with a parallel plate transmission line and the short circuit at the bottom of corrugation is transformed to an open circuit at the corrugation opening if the depth of corrugation is an odd multiple of a quarter wavelength. This open circuit is equivalent to a zero tangential magnetic field at the corrugation opening, which is the characteristic of a PMC.

Due to their characteristics, AMCs may be used as the ground planes of antennas to achieve multipath resistant radiation patterns. Although AMCs do not generally block the propagation of TE surface waves, this is not often a concern as the cut-off frequency of TE modes is usually much higher than the frequency of operation in the microwave regime. For instance, from 2.1,

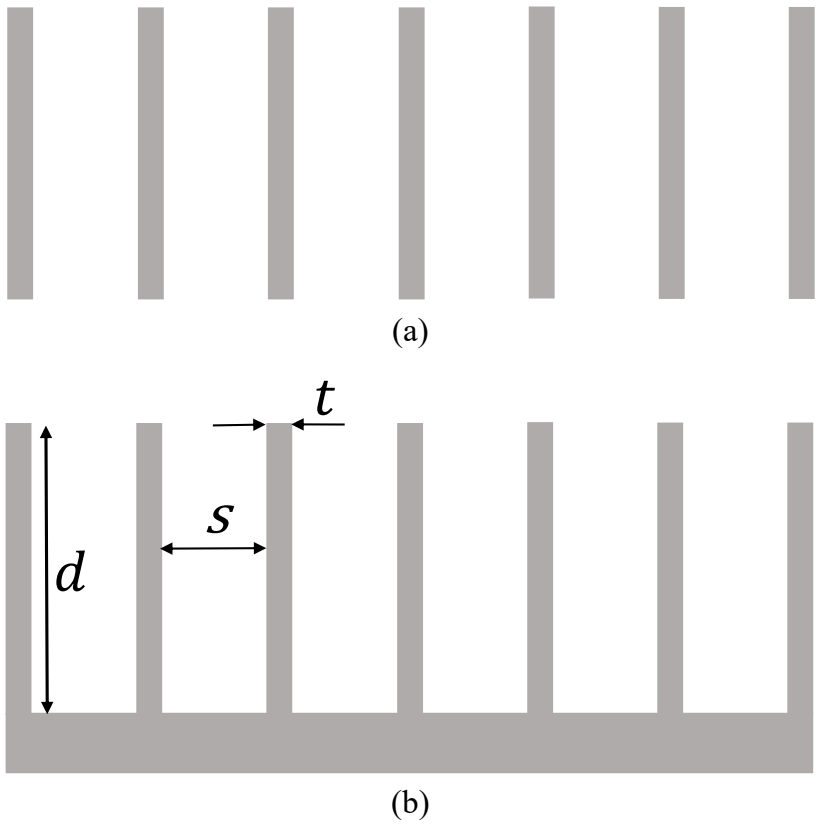

Figure 2.3: A corrugated surface, and example of an AMC when $s + t << \lambda$ and $d = \lambda/4$ (a) Top view (b) Front view.

the cut-off frequency of the TE_1 mode for an FR4 substrate with thickness of 3 mm and permittivity of 4.4, is roughly 40.67 GHz which is higher than the frequency of operation for most microwave applications.

2.3.2 Soft Surfaces

A soft surface is characterized by blocking the propagation of TE and TM surface waves, simultaneously [20]. An example of a soft surface is a surface formed by repetition of PEC and PMC strips where PEC and PMC strips block the propagation of TE and TM surface waves, respectively. Consequently, the corrugated surface depicted in Fig. 2.3 is not only an AMC, but also is a soft surface for the waves propagating perpendicular to the corrugations. A more practical version of this corrugated surface, is a corrugated metallic disk with concentric circular corrugations, also known as choke rings, as illustrated in

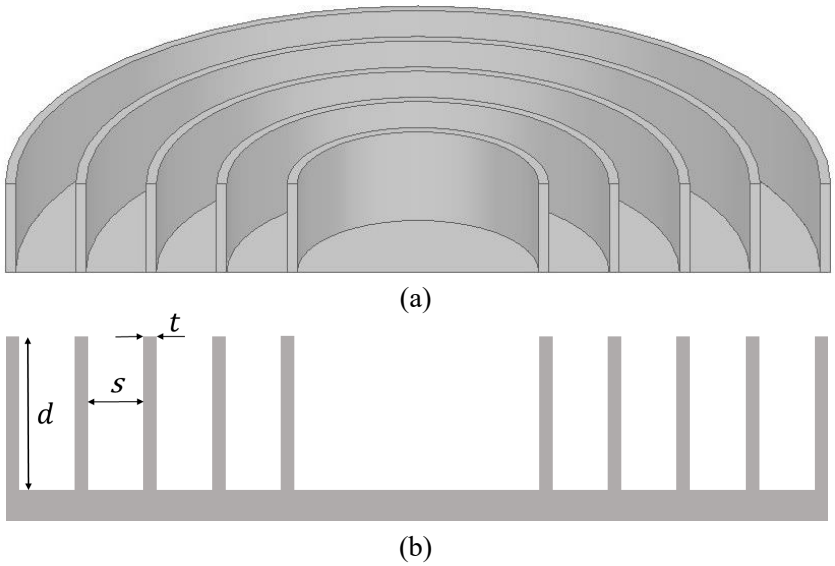

Figure 2.4: A choke ring structure, and example of a soft surface when $s+t << \lambda$ and $d = \lambda/4$ (a) Isometric view (b) Cross section.

Fig. 2.4. Due to radial symmetry, a choke ring structure is a soft surface for waves propagating in any direction.

2.3.3 Electromagnetic Band-Gap Structures (EBGs)

An EBG is a 2D periodic surface which prevents the propagation of SWs by providing a band-gap. Fig. 2.5 shows an example EBG surface (known as mushroom-like EBG) which consists of an array of metallic patches connected to a flat metallic sheet through a series of vias. If the mushroom-like unit cell, shown in Fig. 2.6, is small compared to the operating wavelength, the unit cell may be modeled with a parallel LC circuit [21], where the capacitance is formed in slots between the metallic patches, whereas, the inductance is formed in the pass between the patches through the vias and the bottom plate. Thus, the structure may be modeled as a 2D network of LC resonators which act as a 2D filter and prevent the propagation of SWs in certain frequencies. In the limit that the cell size is much smaller than wavelength, the surface may be assigned a surface impedance equal to the impedance of the unit cell equivalent LC resonator, $Z_s = j\omega L/1 - \omega^2 LC$. Near the resonance frequency, the surface impedance is high meaning the tangential magnetic field is small.

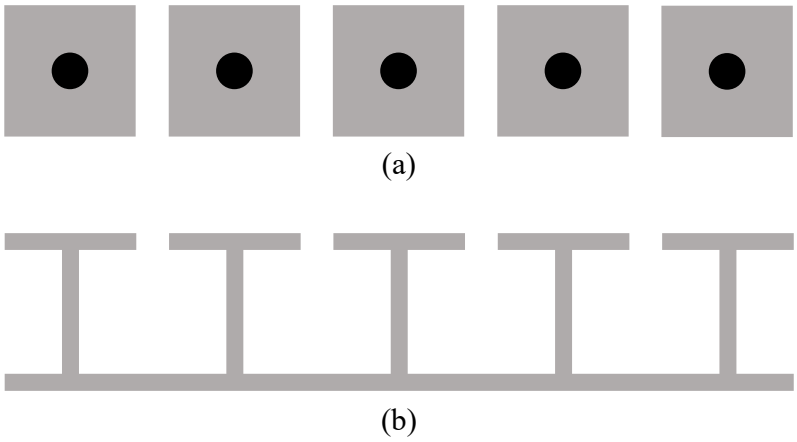

Figure 2.5: An EBG structure (a) Top view (b) Front view.

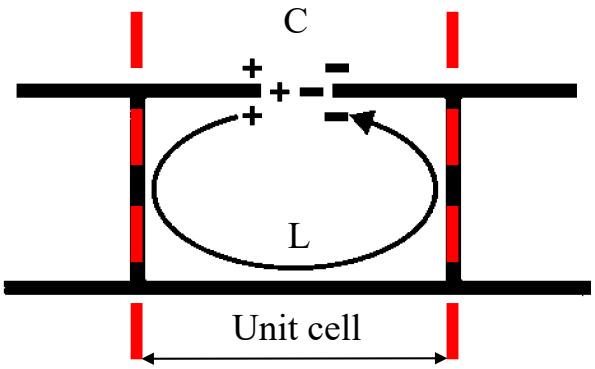

Figure 2.6: Illustration of capacitance and inductance in the unit cell of the mushroom-like EBG.

Consequently, the structure shows AMC characteristics as well.

2.3.4 High-Impedance Surfaces (HISs)

In order to describe the high-impedance surfaces and their behavior in interaction with surface waves, first, we briefly analyze the propagation of surface waves on a general impedance surface. Fig. 2.7 depicts the propagation of TM and TE surface waves over a surface with given surface impedance of Z_s. For the TM case, assuming propagation along the y-axis and the impedance surface being located on the x-y plane, the electric and magnetic fields can be written as:

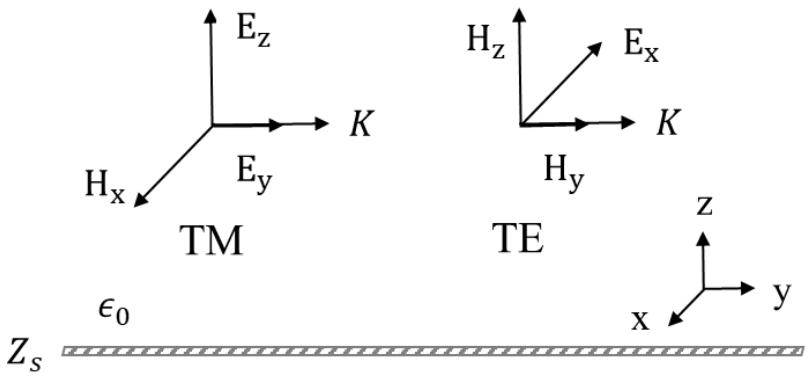

Figure 2.7: Propagation of surface waves over a general impedance surface.

$$E_y = E_{y0}\, e^{-\alpha z - jk_y y}$$

$$E_z = E_{z0}\, e^{-\alpha z - jk_y y}$$

$$H_x = H_{x0}\, e^{-\alpha z - jk_y y} \tag{2.3}$$

where α is the attenuation constant along the z-axis. Following [22], we use the Maxwell's equation $\nabla \times H = j\omega\epsilon_0 E$ to obtain the relationship between E_{y0}, E_{z0}, and H_{x0}. Applying this identity results in:

$$-\alpha H_{x0} = j\omega\epsilon_0 E_{y0} \tag{2.4}$$

$$k_y H_{x0} = \omega\epsilon_0 E_{z0} \tag{2.5}$$

Hence, the surface impedance can be obtained as:

$$Z_s = \frac{E_y(z=0)}{H_x(z=0)} = \frac{j\alpha}{\omega\epsilon_0} \tag{2.6}$$

Assuming that Z_s is given and imposed by the impedance surface, the above equation can be re-written as:

$$\alpha_{\mathrm{TM}} = -j\omega\epsilon_0 Z_s \tag{2.7}$$

The TE case can be analyzed in a similar approach which results in:

$$Z_s = -\frac{E_x(z=0)}{H_y(z=0)} = -\frac{j\omega\mu_0}{\alpha} \tag{2.8}$$

which can be re-written as:

$$\alpha_{\mathrm{TE}} = -\frac{j\omega\mu_0}{Z_s} \tag{2.9}$$

It worth noting that to obtain the correct sign for the surface impedance, one should pay attention to the convention that an absorbing surface should posses positive resistance whereas a reflective one should have a negative resistance [22]. The minus sign in 2.8 is considered for the surface impedance of TE wave to comply with this convention.

For the surface wave to exist, α must be a positive real number. In contrast, a negative α means that the solution is invalid and the surface wave cannot propagate on the surface. Thus, a TM surface wave is supported when Z_s is inductive and is stopped when it is capacitive. In contrary, a TE surface wave is supported when Z_s is capacitive and is stopped when it is inductive. One may conclude that no surface is able to block the propagation of TE and TM surface waves at the same time, however, this incorrect allegation, arises from the fact that surface impedance is in fact an average surface impedance associated with a smoothed surface, which is an approximation of the actual textured surface. That is why a corrugated surface is able to suppress the propagation of TE and TM surface waves at the same time while it demonstrates a capacitive average surface impedance. In the corrugated structure of Fig. 2.3, the surface impedance over the metallic strips is approximately zero. Thus, the average surface impedance of a unit cell is obtained from:

$$Z_s = j\frac{s}{s+t}Z_0 \tan(\beta d) \tag{2.10}$$

Where $jZ_0 \tan(\beta d)$ is the input impedance of the equivalent transmission line of the corrugation (with Z_0 being the characteristic impedance of the parallel-plate transmission line and β the propagation constant), and $s/s+t$ is called the filling factor. One may observe that although Z_s is capacitive for $\lambda/4 < d < \lambda/2$ (recall $\beta = 2\pi/\lambda$), the TE surface waves are suppressed by teeth of the corrugated structure regardless of the depth of corrugations. Thus, the surface impedance model shows limitations in predicting the complete behavior of a textured surface. Despite the limitations, the concept of surface impedance

is useful in designing textured surfaces since it can be calculated in the unit cell simulations employing simulation software packages. However, one should notice that to suppress TM surface waves, the actual requirement is to enforce the tangential magnetic field to be zero (or small in practice). Therefore, to suppress the TM surface waves the surface impedance should be highly capacitive, i.e., $Z_s = -j|Z_s|$, $|Z_s| >> \eta_0$, where $\eta_0 = \sqrt{\mu_0/\epsilon_0}$ is the intrinsic impedance of free-space. A surface that demonstrates such characteristics is sometimes called a high-impedance surface (HIS). One may notice that HIS is not in fact a different category of surface wave suppressing structures, but is a concept and model to facilitate the design and analysis of such structures. That being said, AMCs, soft surfaces, and EBGs may be called HIS as well.

It worth noting here that if Z_s is highly inductive, α is a positive large number meaning TM surface waves can propagate along the surface and are tightly bound to it. Thus, they diffract when they reach the edges of the surface as it is not infinite in practice.

2.4 Choke Rings and their Applications

As mentioned in subsection 2.3.2, a choke ring structure is a corrugated metallic disk (see Fig. 2.4) which is capable of suppressing TE and TM surface waves at the same time. Due to their surface suppressing characteristics, choke rings have remained the dominant multipath mitigating ground structures in high-precision GNSS antennas. In addition to GNSS applications, choke rings are used in different pattern-shaping problems. In this section, a few examples of the other applications of choke rings are reviewed. In [23], choke rings are employed around an open-ended circular waveguide to obtain a choke horn antenna with hemispherical pattern, stable phase center, and reduced low-elevation multipath for deep space satellite applications, e.g., LEO, MEO, and GEO. The proposed antenna may also be employed as a feed for reflector antennas to increase gain and decrease back-radiation. Another variant of a choke horn antenna is designed in [24] for Q-band radio astronomy applications. The antenna has demonstrated high gain, symmetrical beam, and low

cross-polarization. In [25] and [26], a set of choke rings with nonlinear heights are used to achieve gain enhancement (compared to uniform length choke ring antennas) and to provide an isoflux-shaped pattern which is advantageous in remote sensing satellites where the antenna should compensate for different signal attenuations that occur due to different satellite angles relative to the ground station. In a novel application, choke rings are used in [27] as a shield to isolate the ground penetrating radar (GPR) antennas from the above-ground environment.

Chapter 3

Proposed Miniaturization Technique and the Introduction of Folded and Multi-Folded Corrugations

As discussed in section 2.3.4 TM surface waves will be suppressed most effectively when the surface impedance becomes highly capacitive. As a result, in the corrugated structure of Fig. 2.3, the corrugation depth, d , should be slightly larger than a quarter-wavelength to bring about the best surface wave suppression. In other words, the resonance frequency of corrugations and surface impedance should be slightly below the intended frequency of operation. This requirement results in different disadvantages for the employment of corrugated structures in GNSS antennas such as large size, heaviness, costly fabrication, and inability to integrate with printed circuit board (PCB) structures. In order to reduce the necessary physical length of corrugations while maintaining the effective electrical length and desired resonance frequency, the author proposes to introduce a discontinuity in form of a fold or slit in each corrugation as shown in Fig. 3.1. The narrow slit excites evanescent higher order modes near the discontinuity and in turn, adds a capacitance in middle of the corrugation. This extra capacitance can decrease the resonance frequency of the corrugation and lead to depth miniaturization.

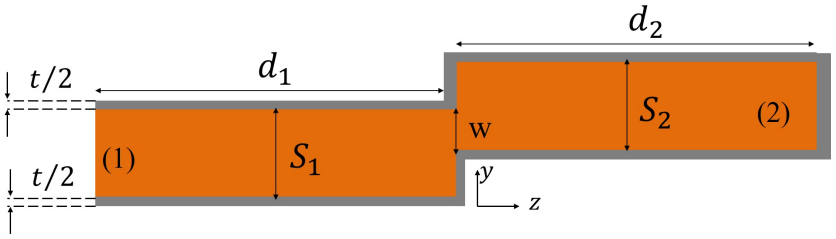

Figure 3.1: Cross section of a folded corrugation (unit cell of a folded corrugated structure).

3.1 Analysis of Folded Corrugations using Modal Expansion Technique

In order to extract the mathematical relationship between the slit capacitance and slit dimensions, and develop a design procedure there after, the folded corrugation is analyzed using the modal expansion method. Following the procedure employed in [28] and [29], with a number of modifications, the equivalent circuit of the folded corrugation can be derived analytically. Fig. 3.1 depicts the unit cell of a periodic structure formed by repetition of folded corrugations. The corrugations are assumed infinitely long in the x-direction and periodic in the y-direction. An oblique plane wave impinges on the corrugated surface, which for the purpose of this analysis, it is assumed to be TM polarized as the interaction of TE plane waves with the structure is negligible [28]. By employing the modal expansion in the parallel plate waveguides of region (1) and (2), the y-component of the electric fields at both sides of the slit can be written as:

$$E_y^{(1)}(y) = \left(1 + R^{(1)} + \sum_{n\neq 0} E_n^{(1)} e^{-jk_n^{(1)} y}\right) e^{-jk_t y} \tag{3.1}$$

$$E_y^{(2)}(y) = \sum_{n=-\infty}^{\infty} E_n^{(2)} e^{-jk_n^{(2)} y} \tag{3.2}$$

where the amplitude of the impinging plane wave has been normalized to unity, $R^{(1)}$ is the reflection coefficient of the reflected plane wave inside region (1), $k_t = (\epsilon_r)^{\frac{1}{2}} k_0 \sin\theta$ is the tangential component of the wavevector of the obliquely incident plane wave, with $k_0 = 2\pi f/c$ being the free-space wavenumber (f is

the frequency of the incident time-harmonic field and the c is the speed of light in free space), and θ the incidence angle. $k_n^{(1)} = 2\pi n/p_1$ and $k_n^{(2)} = 2\pi n/p_2$ are the cutoff wavenumbers of higher order modes, where $p_1 = s_1 + t$ and $p_2 = s_2 + t$ represent preiodicity intervals in region (1) and (2), respectively. The coefficients of the field expansions can be derived by projecting each mode over the field profile using Fourier analysis. In the language of mathematics:

$$E_n^{(1)} = \frac{1}{p_1} \int_{p_1} E_y^{(1)}(y) e^{j(k_n^{(1)} + k_t)y} dy \tag{3.3}$$

$$E_n^{(2)} = \frac{1}{p_2} \int_{p_2} E_y^{(2)}(y) e^{jk_n^{(2)} y} dy \tag{3.4}$$

It worth reminding that the tangential electric field on a perfect electric conductor is zero and practically, the integration in (3.3) and (3.4) happens only over the slit. Due to the narrow width of the slit, the spacial profile of the field over it can be assumed independent of frequency [29]. In other words, $E_y(y) = A(f)g(y)$ where $g(y)$ is the frequency-independent spacial profile of the field and $A(f)$ is the frequency-dependent amplitude of the field. For TM polarized incident plane waves, the spacial field profile can be written as [29]:

$$g(y) = \left[1 - (\frac{y - \frac{w}{2}}{\frac{w}{2}})^2\right]^{-\frac{1}{2}}, 0 < y < w \tag{3.5}$$

which takes into account the singularities at the edges of the slit. By substituting (3.5) in (3.3) and (3.4), the coefficients of the field expansion are obtained as:

$$E_n^{(1)} = \frac{w}{p_1} A(f) J_0((k_n^{(1)} + k_t)\frac{w}{2}) e^{j(k_n^{(1)} + k_t)\frac{w}{2}} \tag{3.6}$$

$$E_n^{(2)} = \frac{w}{p_2} A(f) J_0(k_n^{(2)}\frac{w}{2}) e^{jk_n^{(2)}\frac{w}{2}} \tag{3.7}$$

where J_0 is the zero-order Bessel function of the first kind. Considering the fact that $1 + R^{(1)} = E_0^{(1)}$, one may obtain:

$$1 + R^{(1)} = \frac{w}{p_1} A(f) J_0(k_t\frac{w}{2}) e^{jk_t\frac{w}{2}} \tag{3.8}$$

In order to derive another relation between $R^{(1)}$ and $A(f)$, and attain an expression for $R^{(1)}$, the continuity of tangential magnetic field over the slit

$(H_x^{(1)} = H_x^{(2)})$, can be projected over the electric field profile. In other words:

$$\int_0^w \Big(A(f)g(y)\Big)^* \Big(H_x^{(1)}(y) - H_x^{(2)}(y)\Big)dy = 0 \tag{3.9}$$

To solve (3.9), the expressions for the tangential magnetic fields at both sides of the slit may be derived from (3.1) and (3.2) as:

$$H_x^{(1)}(y) = \left(1 - Y_0^{in,(1)}R^{(1)} - \sum_{n\neq 0} Y_n^{in,(1)}E_n^{(1)}e^{-jk_n^{(1)}y}\right)e^{-jk_t y} \tag{3.10}$$

$$H_x^{(2)}(y) = \sum_{n=-\infty}^{\infty} Y_n^{in,(2)}E_n^{(2)}e^{-jk_n^{(2)}y} \tag{3.11}$$

where $Y_n^{in,(i)}$ is the input admittance of the transmission line associated with the n^{th} harmonic in the i^{th} medium, that can be obtained from:

$$Y_n^{in,(1)} = Y_n^{(1)}\frac{Y_n^{(0)} + jY_n^{(1)}\tan(\beta_n^{(1)}d_1)}{Y_n^{(1)} + jY_n^{(0)}\tan(\beta_n^{(1)}d_1)} \tag{3.12}$$

$$Y_n^{in,(2)} = -jY_n^{(2)}\cot(\beta_n^{(2)}d_2) \tag{3.13}$$

where $Y_n^{(i)}$ is the characteristic admittance corresponding to the n^{th} mode in the i^{th} medium, and may be written as:

$$Y_n^{(i)} = \frac{\epsilon_r^{(i)}k_0}{\eta_0\beta_n^{(i)}}, i = 0, 1, 2 \tag{3.14}$$

with $\eta_0 = \sqrt{\mu_0/\epsilon_0}$ being the intrinsic impedance of free-space. $\beta_n^{(i)}$ is the phase constant of the n^{th} harmonic in the i^{th} medium and can be obtained from:

$$\beta_n^{(i)} = \sqrt{\epsilon_r^{(i)}k_0^2 - (k_t + k_n^{(1)})^2}, i = 0, 1 \tag{3.15}$$

$$\beta_n^{(2)} = \sqrt{\epsilon_r^{(2)}k_0^2 - (k_n^{(2)})^2} \tag{3.16}$$

By substituting (3.10) and (3.10) in (3.9), the following relationship between $R^{(1)}$ and $A(f)$ can be derived:

$$\frac{1 - R^{(1)}}{A(f)}Y_0^{(1)}J_0(k_t\frac{w}{2})e^{-jk_t\frac{w}{2}} = \tag{3.17}$$

$$\frac{w}{p_1}\sum_{n\neq 0} Y_n^{in,(1)} J_0^2\Big((k_t+k_n^{(1)})\frac{w}{2}\Big)+\frac{w}{p_2}\sum_{n=-\infty}^{\infty} Y_n^{in,(2)} J_0^2\Big(k_n^{(2)}\frac{w}{2}\Big)$$

Solving (3.8) and (3.17) for $R^{(1)}$ results in:

$$R^{(1)}=\frac{Y_0^{(1)}-(A_0^{(2)}Y_0^{in,(2)}+Y_{eq})}{Y_0^{(1)}+(A_0^{(2)}Y_0^{in,(2)}+Y_{eq})} \tag{3.18}$$

where

$$Y_{eq}=\sum_{n\neq 0}\Big(A_n^{(1)}Y_n^{in,(1)}+A_n^{(2)}Y_n^{in,(2)}\Big) \tag{3.19}$$

$$A_n^{(1)}=\frac{J_0^2\Big((k_t+k_n^{(1)})\frac{w}{2}\Big)}{J_0^2\Big(k_t\frac{w}{2}\Big)}, n\neq 0 \tag{3.20}$$

$$A_n^{(2)}=\frac{p_1}{p_2}\frac{J_0^2\Big(k_n^{(2)}\frac{w}{2}\Big)}{J_0^2\Big(k_t\frac{w}{2}\Big)} \tag{3.21}$$

By comparing (3.18) to the input reflection coefficient of a transmission line, one may interpret that Y_{eq} is connected in parallel with the input admittance of the transmission line associated with the propagation of main harmonic in medium (2), while the characteristic admittance of this transmission line is adjusted by the factor $A_0^{(2)}$. This interpretation is depicted in Fig. 3.2. It worth mentioning that although $A_0^{(2)}$ is generally frequency-dependent, in practice, the slit width is much smaller than a wavelength over the bandwidth of interest, i.e. $w << \lambda^{(1)}$ ($\lambda^{(i)}=\frac{c}{f\sqrt{\epsilon_r^{(i)}}}$ is the wavelength in the i^{th} medium). As a result, $J_0^2\Big(k_t\frac{w}{2}\Big)\approx 1$, which leads to the frequency-independent relation, $A_0^{(2)}\approx p_1/p_2$. Thus, the equivalent circuit remains almost linear over the intended frequency band.

Equation (3.19) describes a parallel combination of transmission lines modeling the higher order modes in Y_{eq}. However, (3.19) can be simplified to admittance of a capacitor. It can be shown that for $p_1<\lambda^{(1)}/2$:

$$\epsilon_r^{(i)}k_0^2-(k_t+k_n^{(1)})^2<0, n\neq 0 \tag{3.22}$$

Similarly, for $p_2<\lambda^{(2)}/2$:

$$\epsilon_r^{(2)}k_0^2-(k_n^{(2)})^2<0, n\neq 0 \tag{3.23}$$

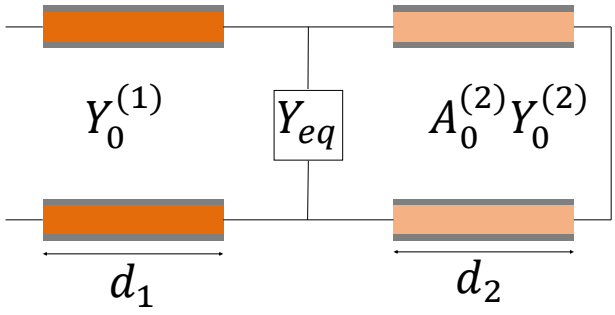

Figure 3.2: Equivalent circuit of the folded corrugated structure

In practice, the required conditions for (3.22) and (3.23) are almost always satisfied, and consequently, $\beta_n^{(i)}$ is purely imaginary for all higher order modes. Thus, (3.15) and (3.16) can be re-written as:

$$\beta_n^{(i)} = -j|\beta_n^{(i)}|, n \neq 0 \tag{3.24}$$

where

$$|\beta_n^{(i)}| = \sqrt{(k_t + k_n^{(1)})^2 - \epsilon_r^{(i)} k_0^2}, i = 0, 1, n \neq 0 \tag{3.25}$$

$$|\beta_n^{(2)}| = \sqrt{(k_n^{(2)})^2 - \epsilon_r^{(2)} k_0^2}, n \neq 0 \tag{3.26}$$

Substituting (3.24) in (3.14) results in:

$$Y_n^{(i)} = j\omega C_n^{(i)}, i = 0, 1, 2 \tag{3.27}$$

where

$$C_n^{(i)} = \frac{\epsilon_0 \epsilon_r^{(i)}}{|\beta_n^{(i)}|}, i = 0, 1, 2 \tag{3.28}$$

Now, by employing (3.24) and (3.27) in (3.12) and (3.13), one may re-write (3.19) as:

$$Y_{eq} = j\omega C_{eq} = j\omega \sum_{n \neq 0} \left(A_n^{(1)} C_n^{in,(1)} + A_n^{(2)} C_n^{in,(2)} \right) \tag{3.29}$$

where

$$C_n^{in,(1)} = C_n^{(1)} \frac{C_n^{(0)} + C_n^{(1)} \tanh(|\beta_n^{(1)}| d_1)}{C_n^{(1)} + C_n^{(0)} \tanh(|\beta_n^{(1)}| d_1)} \tag{3.30}$$

$$C_n^{in,(2)} = C_n^{(2)} \coth(|\beta_n^{(2)}| d_2) \tag{3.31}$$

One may notice that the calculation of C_{eq} from (3.29), apparently requires the calculation of an infinite summation. However, due the characteristics of the Bessel functions, $A_n^{(i)}$ decreases as n increases. Also, $C_n^{(i)}$ and in turn $C_n^{in,(i)}$ decrease as n increases. As a result, C_{eq} can be computed with negligible error using a limited number of terms of the summation in (3.29).

3.2 Demonstration of Miniaturization Capability of Folded Corrugations

As demonstrated in section 3.1 a folded corrugation may be modeled as two transmission lines with a capacitor connected between them. The input impedance of such a configuration is simulated using Keysight ADS, and is compared to the input impedance of a regular (non-folded) transmission line of the same length. As shown in Fig. 3.3, the equivalent circuit of the folded corrugation demonstrates a lower resonance frequency in the input impedance; proving the miniaturization capability of this technique. It should be noted that the impedances are normalized with respect to $j\eta_0$.

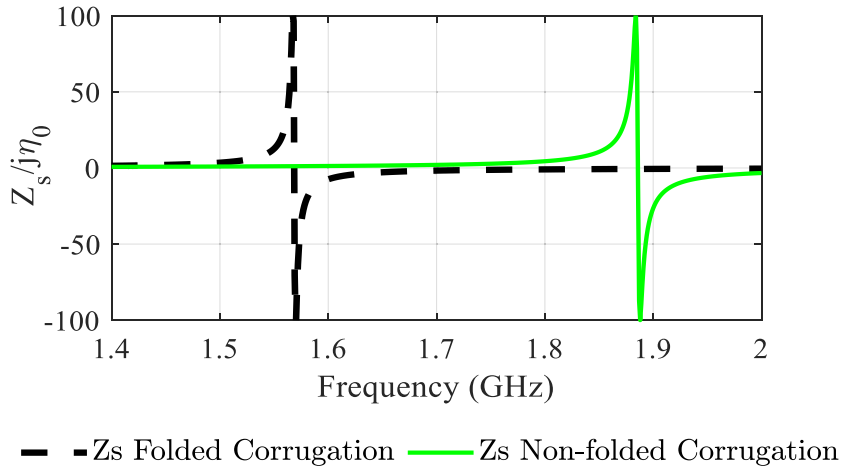

Figure 3.3: Comparison between the normalized surface impedance of a non-folded corrugation and a folded one for $d_1 = d_2 = 9.2$ mm, $\epsilon_r = 4.7$, $C_{\text{eq}} = 0.35$ pF.

3.3 Parametric Analysis of Folded Corrugations

To investigate the effect of corrugation parameters on the value of C_{eq}, a MATLAB code has been developed to calculate C_{eq}. For simplicity, it is assumed that $S_1 = S_2 = S$, and subsequently, $p_1 = p_2 = p$. The value of C_{eq} with respect to slit width, w, has been plotted in Fig. 3.4 for different values of corrugation width, S. It may be concluded from Fig. 3.4 that for a constant corrugation width, C_{eq} increases as slit width decreases. Also, for a fixed slit width, C_{eq} increases as corrugation width increases.

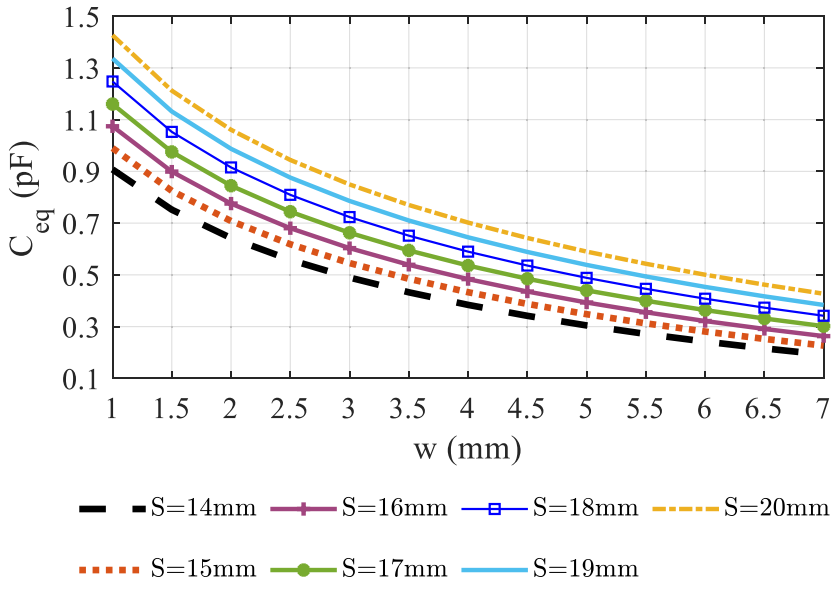

Figure 3.4: Value and variation of C_{eq} for different values of slit width and corrugation width assuming $\epsilon_r = 4.7$, $d_1 = d_2 = 9.2$ mm.

3.4 Multi-Folded Corrugations and their Equivalent Circuit

As demonstrated earlier in this chapter, introducing a fold or slit in a corrugation reduces its resonance frequency and leads to miniaturization of depth of corrugations and height of choke rings. In this section, to achieve further miniaturization, the idea of folded corrugations has been expanded to multi-

Figure 3.5: A multi-folded corrugation.

folded corrugations (MFCs), as illustrated in Fig. 3.5. The equivalent circuit of MFCs may be derived following a similar procedure as described in section 3.1. However, deriving expressions for $Y_n^{\text{in},(i)}$ for MFCs is a cumbersome process due to the fact that a greater number of mediums are involved. To address this challenge, a reasonable approximation is made in this work. For the purpose of calculation of $Y_n^{\text{in},(i)}$, it is assumed that the slit is placed between two semi-infinite parallel plate waveguides. This assumption leads to:

$$C_n^{\text{in},(i)} \approx C_n^{(i)}, i = 1, 2 \tag{3.32}$$

This approximation may be justified in two ways. From the viewpoint of mathematics, the arguments of tangent hyperbolic and cotangent hyperbolic functions in (3.30) and (3.31) are usually sufficiently large to assume:

$$\tanh(|\beta_n^{(1)}|d_1) \approx 1, \coth(|\beta_n^{(2)}|d_2) \approx 1 \tag{3.33}$$

On the other hand, from the electromagnetic point of view, the lengths d_1 and d_2 are large enough to allow higher order modes to decay substantially before they reach to free-space or short circuit at the borders of regions (1) and (2). Consequently, the free-space and short circuit at the end of regions (1) and (2) do not alter the decaying fields of higher order modes considerably. As a result, the capacitance created by higher order modes around the slit is almost independent of the loads placed at the end of parallel plate waveguides. Thus, C_{eq} may be approximated as:

$$\widetilde{C}_{\text{eq}} \approx \sum_{n\neq 0} \left(A_n^{(1)} C_n^{(1)} + A_n^{(2)} C_n^{(2)} \right) \tag{3.34}$$

where the tilde over the C_{eq}, denotes to the approximated value. To test the validity of this approximation, the relative error of $\widetilde{C}_{\text{eq}}$ with respect to C_{eq}, which is defined as:

$$\text{Error}_{C_{\text{eq}}} = \frac{C_{\text{eq}} - \widetilde{C}_{\text{eq}}}{C_{\text{eq}}} \times 100 \tag{3.35}$$

is plotted in Fig. 3.6 versus d (assuming $d_1 = d_2 = d$) for different values of slit width. As Fig. 3.6 illustrates, the error of this approximation is negligible. Thus, to design MFCs, it may be assumed that the equivalent capacitance of all slits are the same and roughly equal to the capacitance of a slit placed between two semi-infinite parallel plate waveguides. By using this approximation, an MFC can be modeled with a number of transmission lines connected through a set of shunt capacitors. For instance, Fig. 3.7 depicts the equivalent circuit of a double-folded corrugation. Such circuit modeling is very useful in obtaining the optimal parameters of an MFC for an intended resonance frequency.

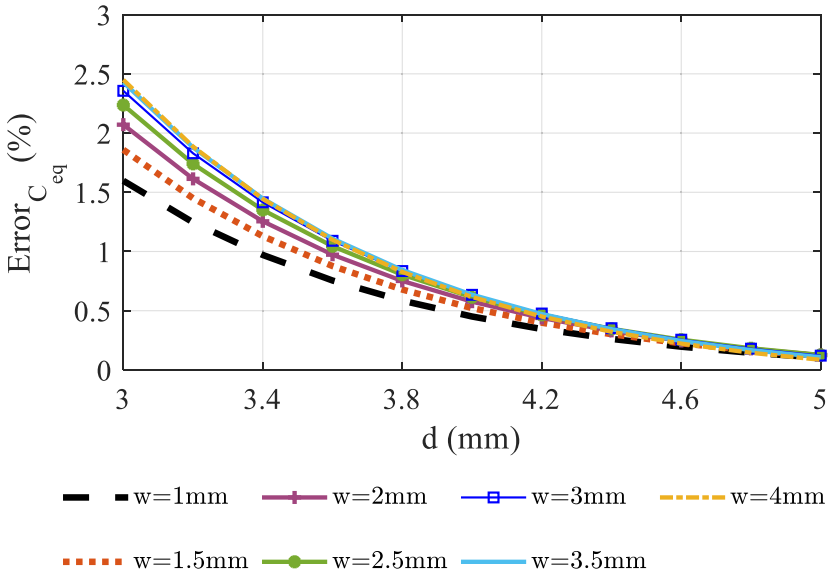

Figure 3.6: Relative error of estimating slit capacitance using ((3.34)).

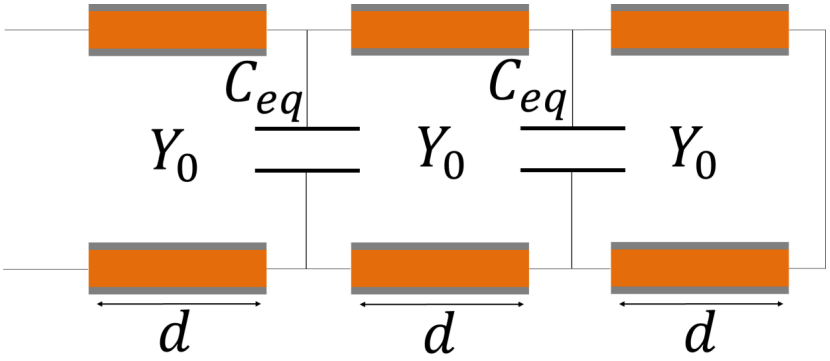

Figure 3.7: Equivalent circuit of a double-folded corrugation.

In order to design a multi-folded corrugated structure, the following procedure may be employed. It should be noted that although the thickness and permittivity of substrates can be different in general, for simplicity, it is assumed here that all substrates posses similar thickness and permittivity.

1) By taking into account the accuracy and limitations of the fabrication technology, and mechanical stability of the design, the minimum practical slit width should be determined (it is assumed 1 mm in this work). Subsequently, the maximum achievable capacitance, given the corrugation width and permittivity of substrate, can be determined using (3.34).

2) By selecting the intended number of layers and utilizing the maximum achievable capacitance in the equivalent circuit of the folded corrugation, the minimum required substrate thickness may be determined by sweeping the input impedance of the equivalent circuit over substrate thickness using circuit simulation software packages.

3) By choosing a practical substrate thickness, close to the minimum required one, and fixing it into the equivalent circuit, the required capacitance to achieve resonance in the desired frequency can then be determined.

4) The proper slit width can be determined by fitting the simulated required capacitance into the plots developed for $\widetilde{C}_{\mathrm{eq}}$.

It worth mentioning that this approach may need to be repeated for a few iterations in order to obtain implementable design parameters.

3.5 Design of Dual-Band Multi-Folded Corrugated Structures

The design of single-band multi-folded corrugated structures discussed in section 3.4. However, in some applications e.g., GNSS multipath suppression, a single-band design may not be sufficient in practice, due to the narrow bandwidth of the resonance. Thus, dual-band multi-folded corrugated structures are needed to obtain surface wave suppression and multipath mitigation over the lower and upper GNSS bands, simultaneously. Fig. 3.8 (a) depicts the unit cell of a dual-band folded corrugated structure. To design a dual-band

folded corrugated structure, one should note that each corrugation resonates at a frequency almost independent of the other one if the intended frequencies for dual-band operation are not too close. Thus, the goal is to set the resonance frequency of each corrugation to the intended frequency of operation (e.g. 1227 MHz and 1575 MHz), using the procedure described in section 3.4. In this case, the periods, p_1 and p_2, are different at both sides of the slit, in contrast to the single-band case in section 3.4. The corrugations correspondent to L1 and L2 frequency bands, are denoted with g_1 and g_2 in Fig. 3.8, respectively. For the former,

$$p_1 = g_1 + t, p_2 = g_1 + t - (w_2^{'} - w_1^{'}) \tag{3.36}$$

and for the later,

$$p_1 = g_2 + t, p_2 = g_2 + t - (w_3^{'} - w_2^{'}) \tag{3.37}$$

This difference must be taken into account when calculating (3.34). It worth mentioning that the single-band case depicted in Fig. 3.1 can be seen as a simplified case of the dual-band design where $g_1 = g_2 = S$, and $w_1^{'} = w_2^{'} = w_3^{'} = w^{'} = S - w$.

Obviously, more than one solution exists as $w_1^{'}$ and $w_2^{'}$ both affect the value of equivalent capacitance related to L1 frequency band, and $w_2^{'}$ and $w_3^{'}$ both impact the one related to L2 frequency band. One possible solution, which is considered in this work, is to assume $w_1^{'} = w_2^{'}$ and find the proper $w_3^{'}$. To design a dual-band multi-folded corrugated surface using this assumption, the following steps may be taken:

1) A single-band corrugated structure should be designed following the procedure described in section 3.4 for each of the intended frequency bands (L1 and L2). The optimum value of $w^{'}$, denoted with $w_{\mathrm{opt}_{\mathrm{S_{L1}}}}^{'}$ and $w_{\mathrm{opt}_{\mathrm{S_{L2}}}}^{'}$, should be recorded as well as their corresponding slit capacitors, $C_{\mathrm{opt}_{\mathrm{S_{L1}}}}$ and $C_{\mathrm{opt}_{\mathrm{S_{L2}}}}$, where subscripts $\mathrm{S_{L1}}$ and $\mathrm{S_{L2}}$ denote to the single-band designs for L1 and L2 frequency bands, respectively.

2) The initial parameters of the dual-band design may be related to the

single-band designs as follows:

$$w'_{1_D} = w'_{2_D} = w'_{S_{L1}}, w'_{3_D} = w'_{S_{L2}} \tag{3.38}$$

$$g_{1_D} = S_{S_{L1}},\ g_{2_D} = S_{S_{L2}} \tag{3.39}$$

where subscript D denotes to the dual-band design. This technique almost preserves the characteristics of the single-band design over L1 frequency band as the dimensions of one of the folded corrugations have remained unchanged. To achieve significant multipath rejection over the L2 frequency band, the dimensions of the other corrugation should be adjusted such that its slit capacitance, $C_{D_{L2}}$, obtains roughly the same value as the slit capacitance of the optimized single-band design for L2 frequency band, $C_{opt_{S_{L2}}}$. In other words, $C_{D_{L2}} = C_{opt_{S_{L2}}}$. To adjust the design, the initial slit capacitance of the second corrugation, $C_{i_{D_{L2}}}$, should be calculated by employing (3.34), (3.36), and (3.37); and compared with $C_{opt_{S_{L2}}}$. If $C_{i_{D_{L2}}} < C_{opt_{S_{L2}}}$ (which is usually the case), w'_{3_D} should be increased to make the slit narrower and increase the capacitance. Also, the width of second corrugation, g_2, may be increased while keeping the slit width constant as discussed in section 3.3 and illustrated in Fig. 3.4. In the case of $C_{i_{D_{L2}}} > C_{opt_{S_{L2}}}$, measures opposite to the aforementioned ones should be taken. By employing these guidelines, the proper value of g_2 and w'_{3_D} can be obtained after a few iterations of calculating $C_{D_{L2}}$ and comparing it with $C_{opt_{S_{L2}}}$. A final full-wave tuning might be needed to optimize the performance, however, the dimensions resulted from this procedure are close to optimal and a very good start point for the full-wave optimization process. The surface impedance of the aforementioned dual-band unit cell is illustrated in Fig. 3.8 (b).

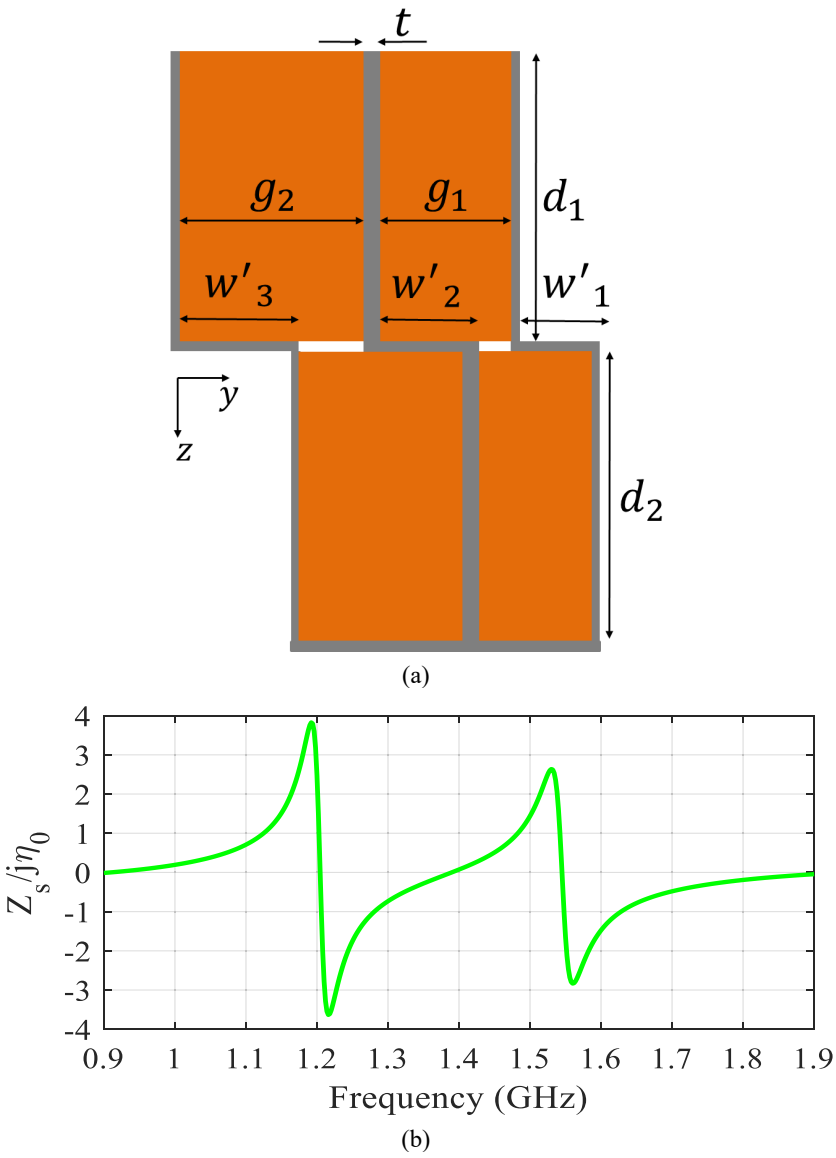

Figure 3.8: (a) Unit cell of a dual-band corrugated structure (b) Normalized surface impedance of the unit cell for $g_1 = 14$ mm, $g_2 = 19$ mm, $w_1{}' = w_2{}' = 9.4$ mm, $w_3{}' = 18$ mm, $t = 2$ mm, $d_1 = d_2 = 7.5$ mm, $\epsilon_r = 4.7$.

Chapter 4

Designed Choke Ring Structures, Results, and Discussion

As discussed earlier, choke rings are 2D corrugated structures that are commonly used as multipath mitigating ground structures in high-precision GNSS antennas. In this chapter, the author's proposed designs, miniaturized substrate integrated choke rings, are presented and their performances are analyzed against conventional choke rings. In order to evaluate the performance of the proposed designs, a dual-band RHCP microstrip patch antenna (NovAtel

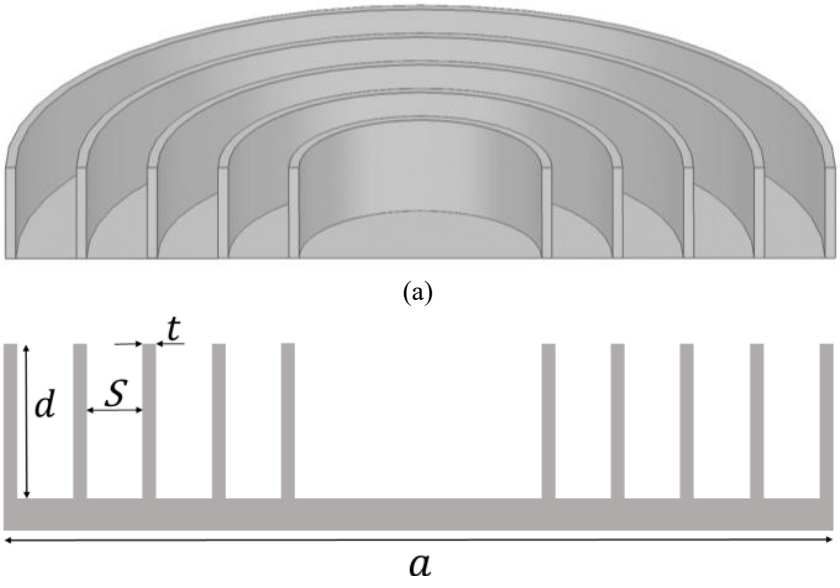

(a)

(b)

Figure 4.1: A conventional choke ring structure (a) Isometric view (b) Cross section and typical dimensions, $a = 342$ mm, $d = 66$ mm, $S = 19$ mm, $t = 6$ mm.

VEXXIS GNSS-502 [30]) is simulated in three scenarios. First, the antenna is simulated by itself. Then, it is mounted on top of the conventional choke ring structure depicted in Fig. 4.1. Finally, the antenna is simulated while it has been mounted on each of the introduced structures. In the two later scenarios the antenna is separated from the choke ring structures with a 5-mm air gap.

4.1 Dual-Band Substrate Integrated Choke Rings

A dual-band substrate integrated choke ring (SICR) structure is designed to suppress surface waves over the L1 and L2 frequency bands. The author's proposed design exploits two corrugations with different depths to satisfy the required corrugation depth over both operating bands. This is realized by using a multilayer structure as illustrated in Fig. 4.2. The top conductor of the bottom layer is engineered such that it acts as the ground plane of the inner corrugation while it is electromagnetically transparent to the outer corrugation. Thus, the depth of the inner corrugation is the sum of the thicknesses of top and middle substrates whereas the depth of the outer corrugation is the sum of the thicknesses of all substrates. It is noteworthy to mention that metallic rings are substituted with via holes covered by the copper cladding

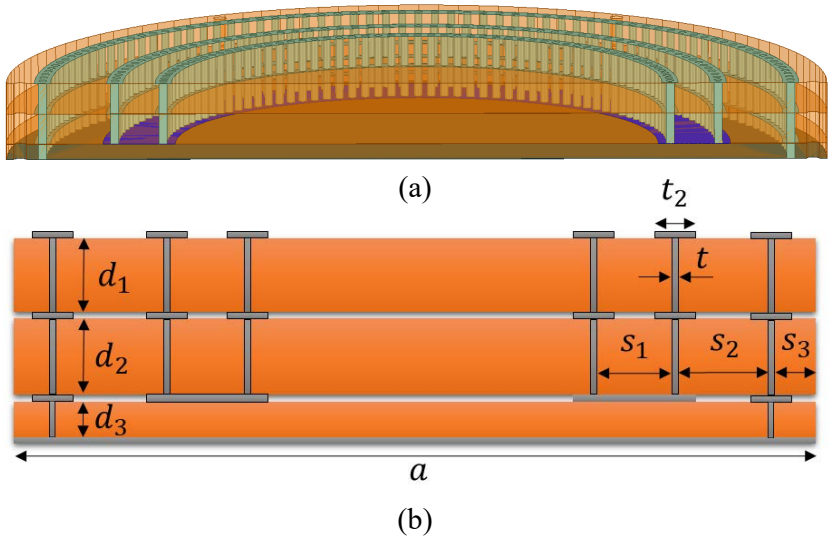

Figure 4.2: (a) Cross section of the SICR (b) Design parameters of the SICR ground structure. $a = 204$ mm, $s_1 = 10$ mm, $s_2 = 16$ mm, $s_3 = 7$ mm, $t = 2$ mm, $t_2 = 4$ mm, $d_1 = d_2 = 7.6$ mm, $d_3 = 3.81$ mm, $\epsilon_r = 9.8$.

of substrates to make the design substrate integrated. The design parameters are given in Fig. 4.2. Three layers of Rogers TMM10i ($\epsilon_r = 9.8$) are used.

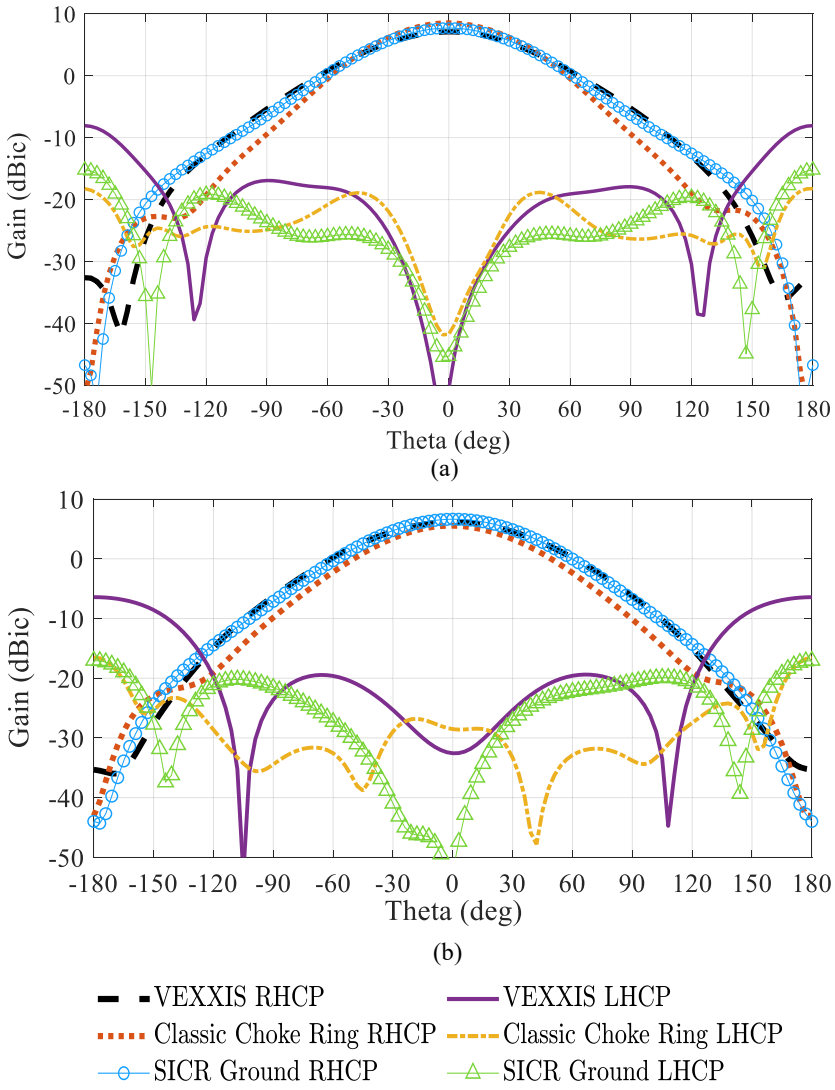

Figure 4.3: Comparison of the radiation patterns of the VEXXIS 502 mounted on the SICR, conventional choke ring, and by itself at (a) 1575 MHz (b) 1227 MHz.

The RHCP and left-handed circularly polarized (LHCP) far-field patterns of the above-mentioned scenarios are compared at the center frequencies of L1 and L2 frequency bands, in Fig. 4.3 (a) and (b) , respectively. It is observed that over the L1 frequency band, the SICR reduces the LHCP gain of the antenna and performs as good as the conventional one. Moreover, the front-to-back ratio has been increased from 15 dB to 23 dB. One may also observe that across the L2 frequency band, the SICR provides an effective multipath rejection. The LHCP gain is below -20 dB and the front-to-back is 23.7 dB

which is 11.2 dB greater than the 12.5 dB provided by the antenna itself. It worth noting that the boresight gain has been improved by 1 dB over both operating bands.

Also, the variation of AR is investigated in the aforementioned scenarios. As illustrated in Fig. 4.4, the SICR lowers the AR of the antenna and keeps it below 3 dB from zenith to horizon over both operating bands which is another proof for its cross-polarization rejection ability.

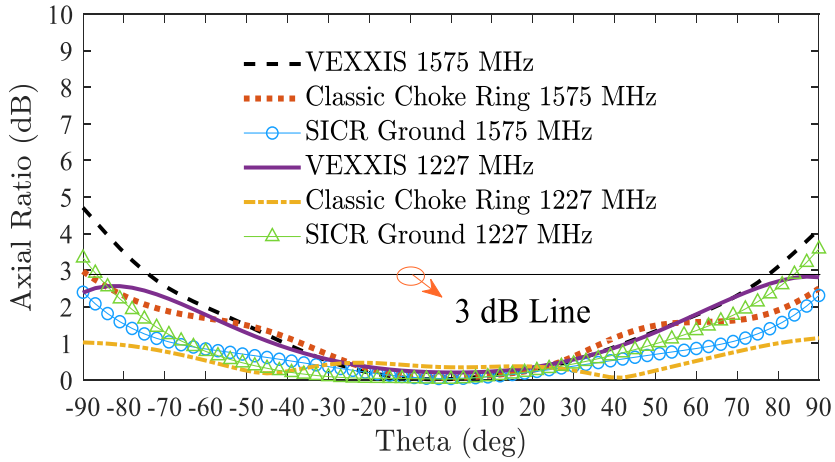

Figure 4.4: Comparison of the ARs of the VEXXIS 502 mounted on the SICR, conventional choke ring, and by itself.

The proposed dual-band SICR delivers light weight fabrication due to its substrate integrated design. The proposed choke ring is about 35% and 70% smaller in height compared to the grooved dielectric one [8] and classic one [7], respectively. It is also 27% and 44% smaller in diameter with respect to the aforementioned designs, [8] and [7], while it demonstrates comparable multi-path suppression characteristics. Therefore, it can be an attractive candidate for low-profile and high-precision GNSS applications.

4.2 Single-Band Folded SICR (FSICR)

A single-band Folded SICR (FSICR) is designed following the procedure described in section 3.4 to suppress the propagation surface waves over the L1 frequency band. The design employs two layers of Rogers TMM10i substrates ($\epsilon_r = 9.8$) with standard thickness of 6.35 mm. The configuration and optimized design parameters are depicted in Fig. 4.5.

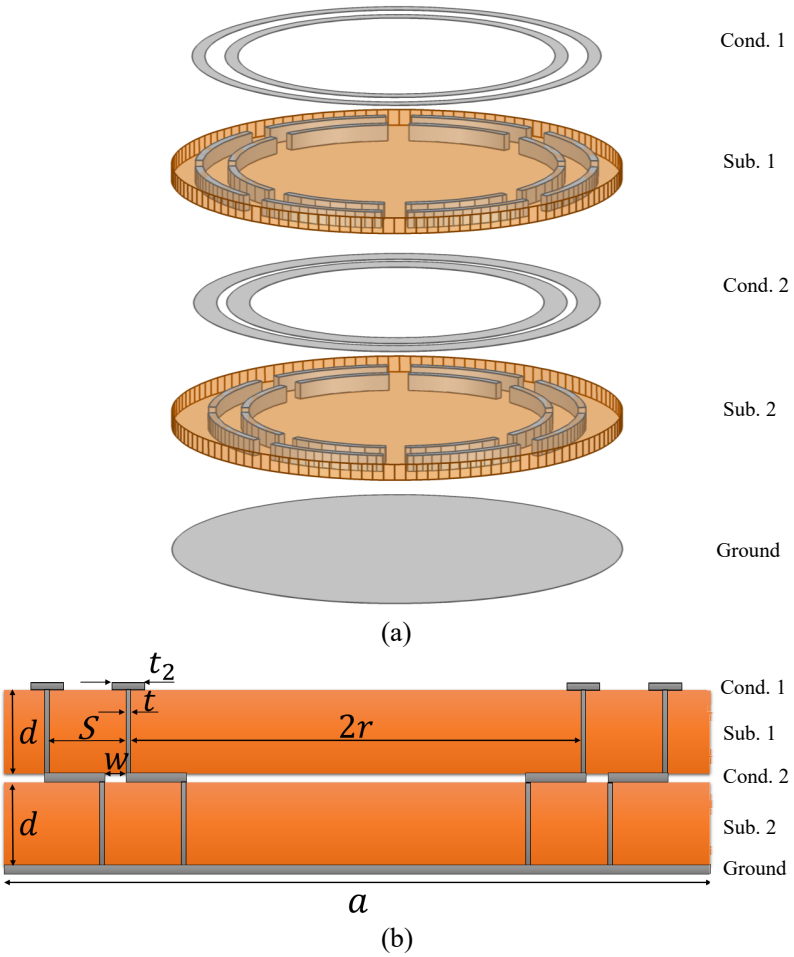

Figure 4.5: Single-band FSICR (a) Expanded view (b) Cross section and design parameters. $a = 178$ mm, $r = 63.5$ mm, $s = 10$ mm, $w = 5$ mm, $t = 3$ mm, $t_2 = 5$ mm, $d = 6.35$ mm, thickness of conductors= 0.018 mm, $\epsilon_r = 9.8$.

The RHCP and LHCP gains of the FSICR are compared against the classic choke ring and antenna itself at 1575 MHz in Fig. 4.6. It is observed that the FSICR reduces the back radiation and performs as good as the classic choke ring. Additionally, the FSICR improves the polarization isolation over the upper hemisphere and outperforms the conventional choke ring in this respect. Polarization isolation enhancement of the FSICR can also be seen in the low AR, illustrated in Fig. 4.7. Although the FSICR outperforms the classic choke ring at the center frequency of L1 frequency band, one should notice that the conventional choke ring provides multipath mitigation over a wide frequency range [7], whereas the FSICR has a narrower operating bandwidth as depicted

in Fig. 4.8. As may observe in Fig. 4.8, the FSICR provides excellent multipath rejection over the L1 frequency band and acceptable multipath rejection over the G1 (1590-1610 MHz) frequency band. However, the performance deteriorates outside of this bandwidth (not shown here). In summary, one may conclude that although the operating bandwidth of FSICR is narrower than the classic choke ring, it covers the upper GNSS frequency bands, L1 and G1.

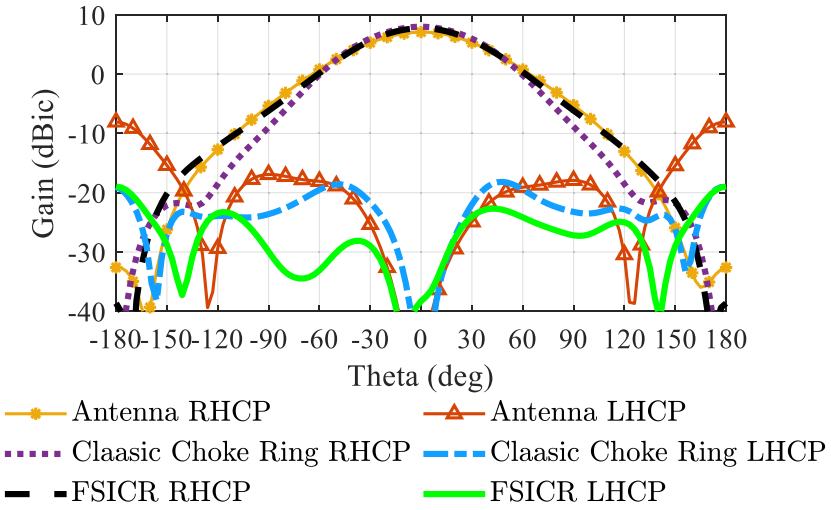

Figure 4.6: Comparison between gains of the antenna when it is mounted on the FSICR, classic choke ring, and by itself at 1575 MHz.

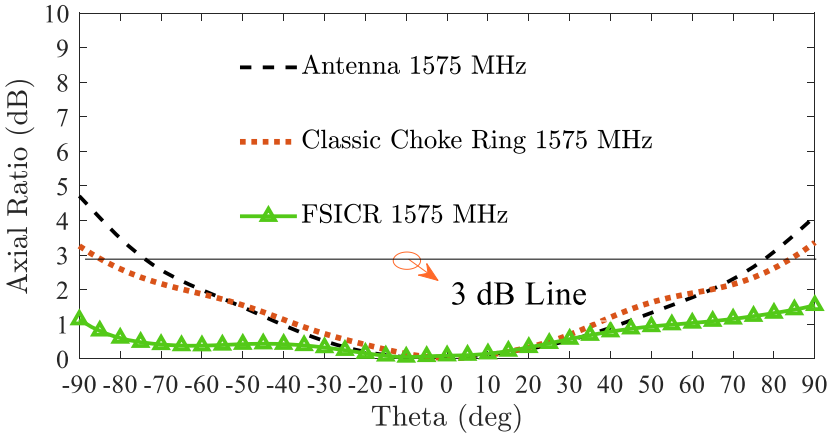

Figure 4.7: Comparison between ARs of the antenna when it is mounted on the FSICR, classic choke ring, and by itself at 1575 MHz.

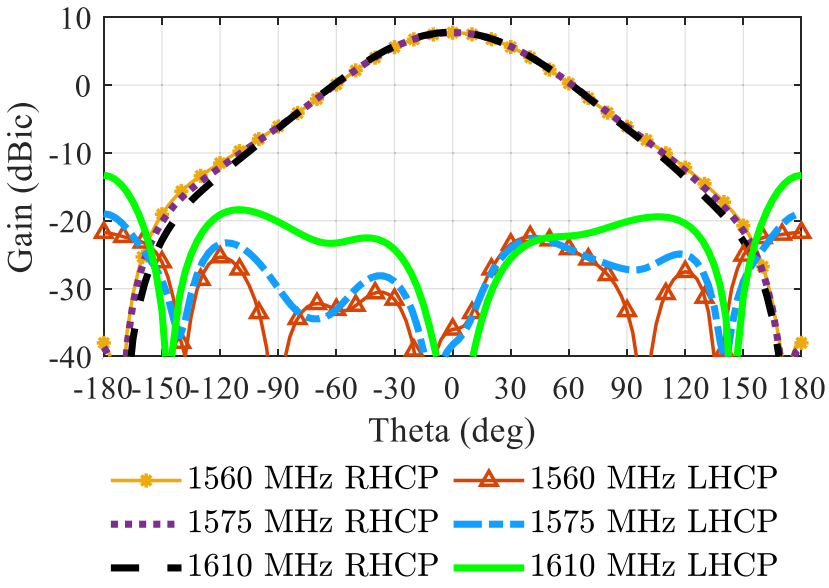

Figure 4.8: Variation of the gain of the antenna mounted on the DFSICR over Upper GNSS frequency band (L1 and G1).

4.3 Dual-Band Double-Folded SICR (DFSICR)

A dual-band Double-Folded SICR (DFSICR) is designed using the design procedure presented in section 3.5 and optimized using the full-wave electromagnetic simulation software, Ansoft HFSS. The optimization goals have been the achievement of a polarization isolation of at least 15 dB (equivalent to AR smaller than 3 dB) over the entire upper hemisphere, and minimization of back radiation. The configuration of the design and the optimized design parameters are illustrated in Fig. 4.9.

4.3.1 Gain and AR

As the first and most important performance metric, the RHCP and LHCP gains of the antenna are plotted for the above-mentioned scenarios at the center frequencies of L1 and L2 frequency bands in Fig. 4.10. Also, AR of the antenna, which is a sign of its polarization isolation, is compared in Fig. 4.11 for the presented scenarios. It is observed that over the L1 frequency band, the DFSICR decreases the LHCP gain of the antenna, reduces back-radiation, and performs as good as the classic choke rings. Also, the DFSICR broadens

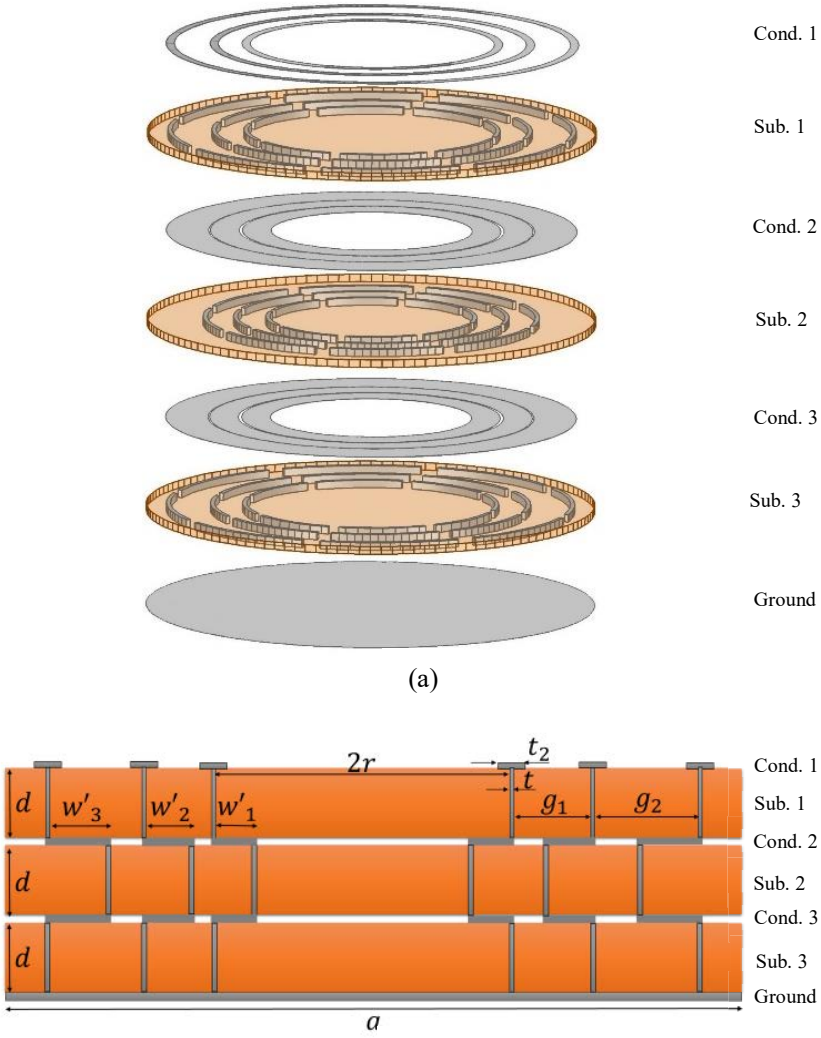

Figure 4.9: Dual-band DFSICR (a) Expanded view (b) Cross section view and design parameters . $a = 227$ mm, $r = 63.5$ mm, $g_1 = 14$ mm, $g_2 = 20$ mm, $w_1{}' = w_2{}' = 11.5$ mm, $w_3{}' = 18.3$ mm, $t = 2$ mm, $t_2 = 4$ mm, $d = 3.2$ mm, thickness of conductors= 0.018 mm, $\epsilon_r = 4.7$.

the 3-dB AR beam-width (ARBW) of the antenna and keeps the AR below 3 dB over the entire upper hemisphere, providing adequate polarization isolation for effective multipath rejection. Over the L2 frequency band, although the polarization isolation is compromised over a narrow range of angles, the LHCP gain and back radiation of the antenna are generally reduced and demonstrate good multipath rejection capabilities.

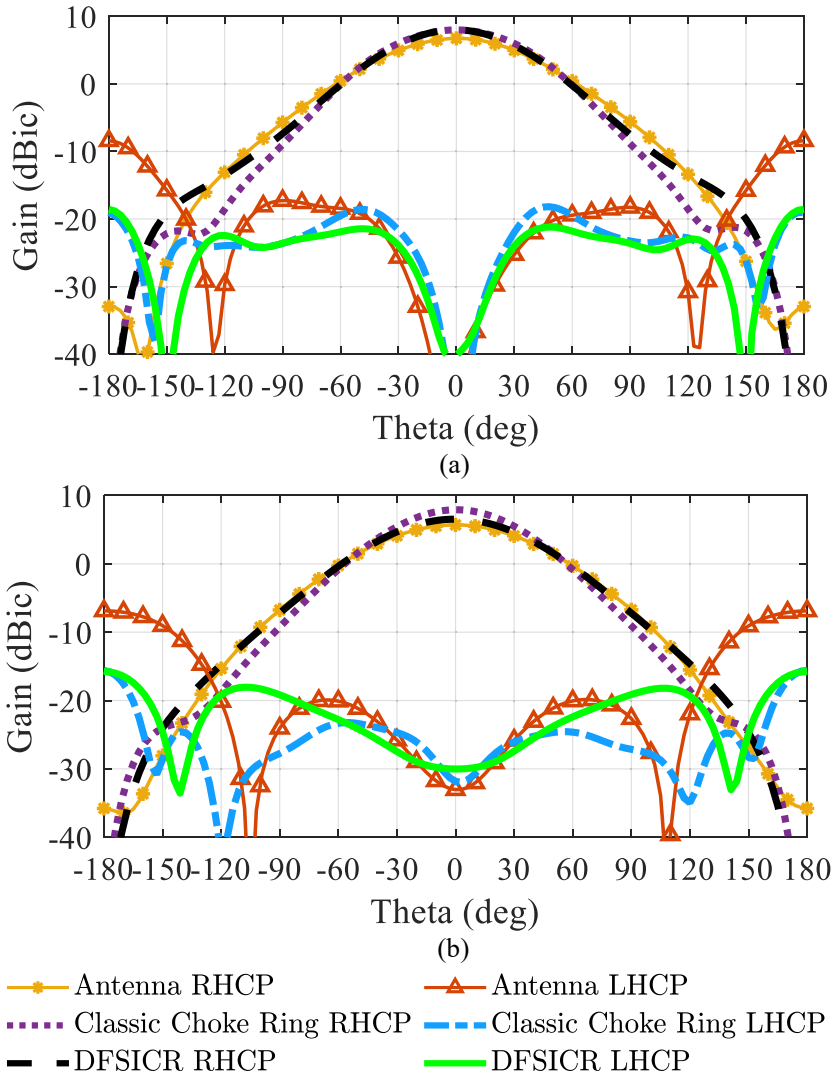

Figure 4.10: Comparison between gains of the antenna when it is mounted on the DFSICR, classic choke ring, and by itself at (a) 1575 MHz (b) 1227 MHz.

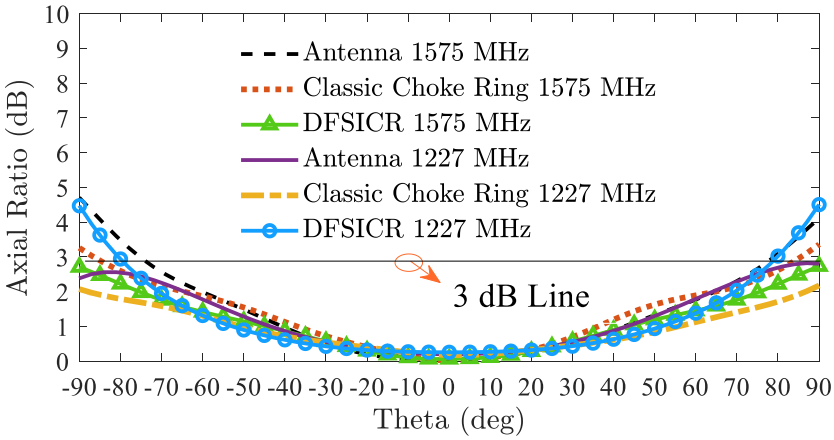

Figure 4.11: Comparison between ARs of the antenna when it is mounted on the DFSICR, classic choke ring, and by itself at (a) 1575 MHz (b) 1227 MHz.

4.3.2 Bandwidth Analysis

In order to assess the frequency bandwidth of DFSICR, the structure has been simulated using discrete frequency sweeps around the design frequencies, 1227 MHz and 1575 MHz. It is observed that the design demonstrates good multipath mitigating characteristics over the entire upper GNSS frequency band, L1 and G1, as well as the L2 frequency bands. The gain of the structure at lower and upper edge of each frequency band is depicted in Fig. 4.12 in addition to the center frequencies. One may observe that over the upper GNSS band, the best performance occurs at the lower edge of the band, 1560 MHz. This is due to the fact that the surface impedance of a choke ring becomes less capacitive as the frequency of operation deviates from the resonance frequency towards higher frequencies. On the other hand, if design parameters are tuned to achieve such performance at the center frequency, performance at the lower edge of the band would suffer severely due to the rapid change of surface impedance from highly inductive to highly capacitive near resonance (one should recall the behavior of surface impedance near resonance in Fig. 3.3). In other words, the lower edge of the band could get located in the highly inductive regime which would result in extreme susceptibility to multipath signals. It worth mentioning that although the level of cross-polarization increases at 1575 MHz and 1610 MHz compared to the 1560 MHz, the achieved front-to-back ratios and polarization isolations are still as good as the conventional choke ring and adequate for effective multipath suppression. A similar behavior can be seen over the L2 frequency band, however, with smaller gain variations. In summary, one may observe that the proposed DFSICR preserves its multipath rejection characteristics over frequency bands necessary to GNSS applications.

4.3.3 Visualization of the Dual-Band Behavior

To better visualize the dual-band behavior of the DFSICR, the amplitude of electric fields on the surface of the structure are plotted in Fig. 4.13 at center frequencies of L1 and L2 frequency bands. As Fig. 4.13 shows, at 1575 MHz the amplitude of the electric field over the inner double-folded corrugation is

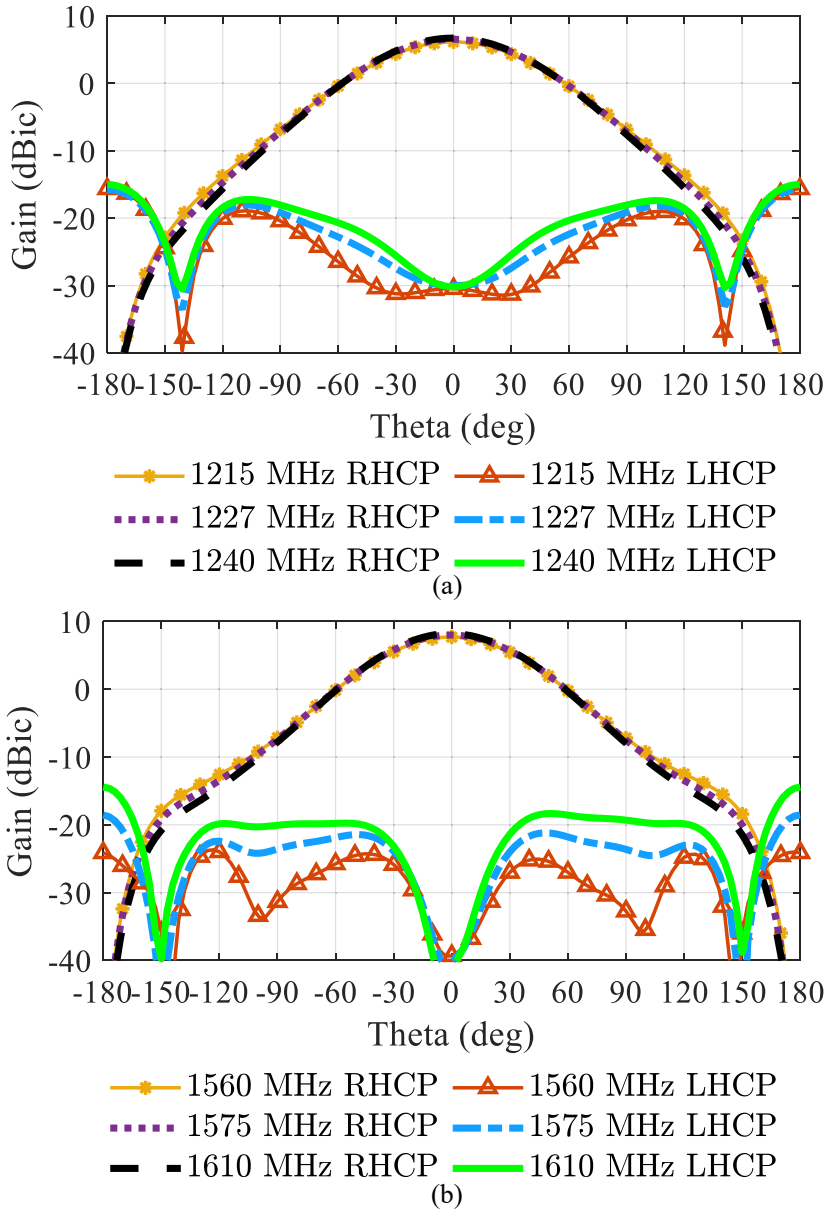

Figure 4.12: Variation of the gain of the antenna mounted on the DFSICR over (a) Upper GNSS frequency band (L1 and G1) (b) L2 frequency band.

significantly higher than the amplitude of the electric field over the outer one. Conversely, at 1227 MHz the electric field demonstrates more strength over the outer corrugation than the inner one. To understand this phenomenon one should recall that at the opening of a short-circuited quarter-wavelength transmission line, the magnetic field has a node whereas the electric field has an anti-node, i.e., the magnetic and electric fields have their minimum and maximum amplitudes, respectively. Thus, the electric field is much stronger over the resonating corrugation.

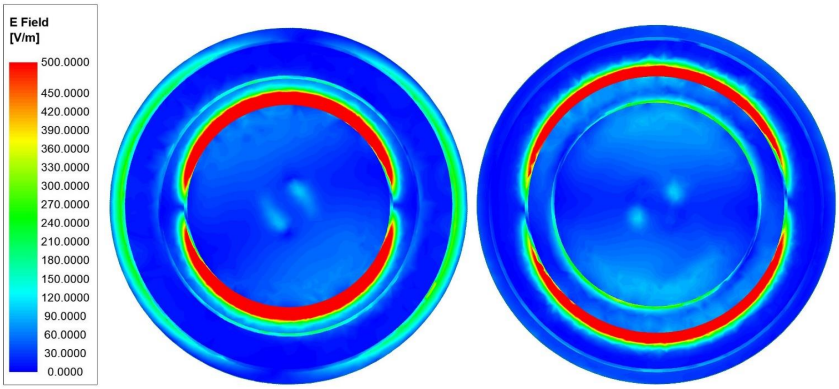

Figure 4.13: Magnitude of electric field over the surface of the dual-band DFSICR at (a) 1575 MHz (b) 1227 MHz.

4.3.4 Study of Slit Parameters

In section 3.3 the effect of slit dimensions on the value of equivalent capacitance was studied theoretically. Here, the effect of slit dimensions on the AR is studied using full-wave electromagnetic simulations and is compared with the expected behavior from the equivalent circuit and surface impedance perspective. As demonstrated earlier, the inner and outer circular double-folded corrugations are mainly responsible for the resonances in surface impedance over the L1 and L2 frequency bands, respectively. Thus, the impact of $w_1^{'}$ and g_1 on AR is studied over the L1 frequency band, whereas, the effect of $w_3^{'}$ and g_2 is analyzed over the L2 frequency band. As mentioned in 3.5, the author has assumed $w_1^{'} = w_2^{'}$ in the design procedure. Hence, $w_2^{'}$ is not an independent variable to consider. The results of this analysis are shown in Fig. 4.14. It can be seen in Fig. 4.14 (a) that as $w_1^{'}$ increases, 3-dB ARBW decreases at the beginning, however, dramatically increases after that, and decreases again there after. This behavior is completely consistent with the equivalent circuit introduced in 3.1. This is because as $w_1^{'}$ increases, the width of the slit in the inner corrugation decreases, which results in higher equivalent capacitance and in turn shifts the resonance towards lower frequencies. As the resonance frequency becomes closer to the intended frequency of operation, the surface impedance becomes highly inductive at first but changes to highly capacitive after that. In the highly inductive regime, the propagation of TM surface

waves is strongly supported, resulting in low polarization isolation and high AR at low-elevation angles. Conversely, in the highly capacitive regime, TM surface waves cannot propagate. Consequently, high polarization isolation is achieved. As $w_1^{'}$ and subsequently C_{eq} further increase, the resonance shifts to frequencies lower than the design frequency. This results in a capacitive but not a highly capacitive surface impedance at the design frequency which in turn cannot suppress TM surface waves very efficiently. Thus, polarization isolation degrades. A similar behaviour is found in the study of $w_3^{'}$ as depicted in Fig. 4.14 (b) which can be justified with the same reasoning. This kind of behavior can be observed in the variations of AR with respect to g_1 and g_2 as well, as illustrated in Fig. 4.14 (c) and (d). One could expect such behavior by recalling the fact that increasing corrugation width while keeping slit width constant, increases C_{eq} as discussed in 3.3. As elaborated earlier in this section, the increase of C_{eq} shifts the resonance towards lower frequencies which results in a degradation-improvement-degradation behavior in performance as C_{eq} continues to increase. It worth mentioning that in analyzing the effect of g_1 and g_2, the $w_1^{'}$ and $w_3^{'}$ have been adjusted in each variation to keep the slit width, $g_1 - w_1^{'}$ and $g_2 - w_3^{'}$, constant. Ultimately, one can conclude from the parametric study presented here that the theoretical analysis provided in section 3.1 is in very good agreement with the result of full-wave simulations.

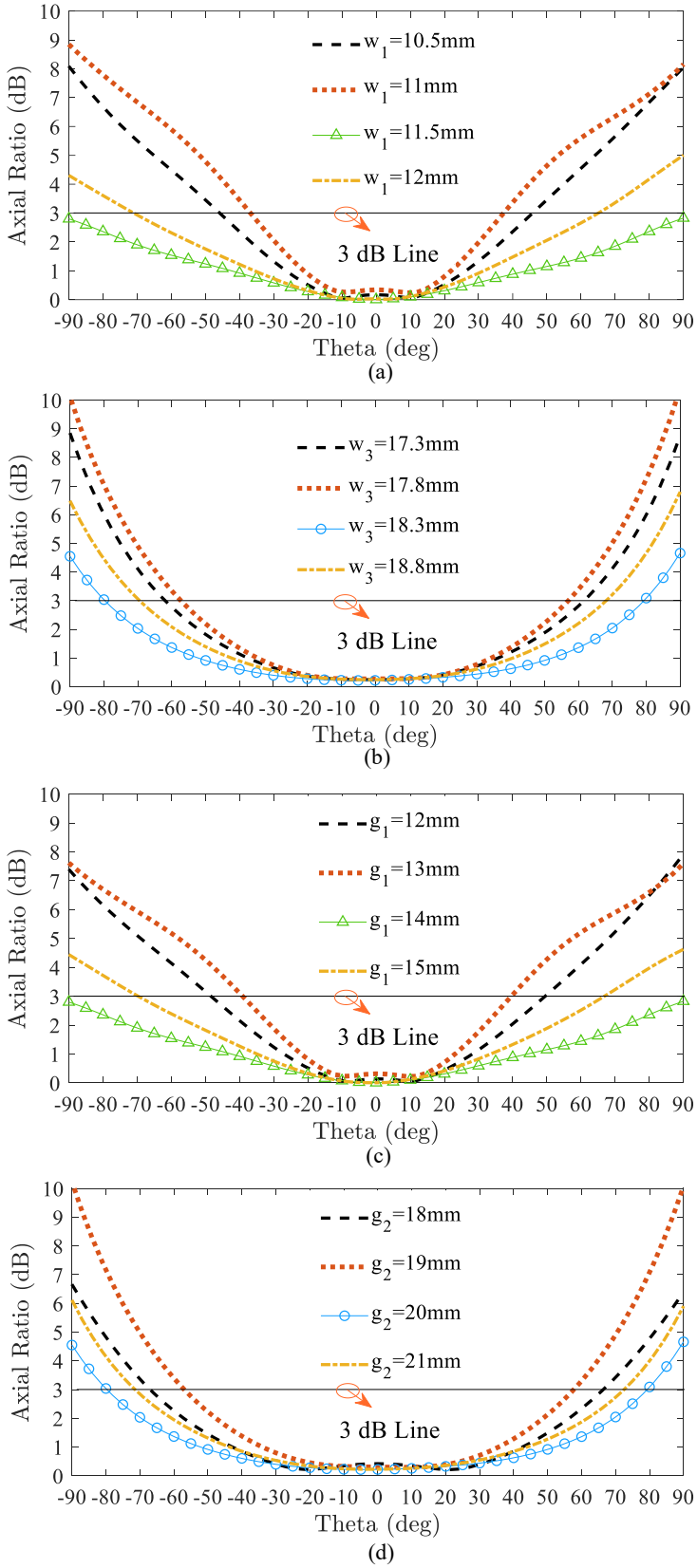

Figure 4.14: Variation of the AR of the antenna mounted on the DFSICR for (a) $w_1^{'}$, 1575 MHz (b) $w_3^{'}$, 1227 MHz (c) g_1, 1575 MHz (d) g_2, 1227 MHz.

4.3.5 Phase Center Stability Analysis

Phase center of an antenna is the center of a hypothetical constant-phase sphere tangential to the far-field radiation of the antenna [7]. The stability of the phase center of the antenna over the operating bandwidth is necessary in high-precision positioning and navigation [1]. Thus, in this section, the impact of the proposed DFSICR on the variation of the phase center of the employed antenna is analyzed. As discussed in [31], phase center of an antenna can be found by finding the center of the best-fit sphere to the three dimensional (3D) phase data. It has been achieved in this work through a least square method. The location of the phase center of the antenna in presence and absence of the DFSICR is given in Table 4.1 for multiple frequencies in the operating bandwidth of the DFSICR. It should be noted that the origin of reference coordinate system is located at the center of the ground plane of the antenna with the z-axis being normal to the antenna. Symbols X_c, Y_c, and Z_c denote to the components of the phase center of the antenna along the x-axis, y-axis, and z-axis, respectively. As Table 4.1 shows, the employment of DFSICR slightly shifts the location of the phase center along the z-axis; however, its peak-to-peak variations over the L2, L1, and G1 frequency bands are limited to 2.79 mm, 3.26 mm, and 1.27 mm, respectively. A peak-to-peak phase ripple of 10°, which is equivalent to peak-to-peak variations of 6.8 mm at 1227 MHz, 5.3 mm at 1575 MHz, and 5.2 mm at 1600 MHz, is considered acceptable in high-accuracy GNSS applications [32]. Therefore, one may conclude that the DFSICR meets the phase center stability requirements of high-precision GNSS antennas.

Table 4.1: Phase center of the antenna in presence and absence of the DFSICR.

Frequency (MHz)	1215	1227	1240	1560	1575	1590	1600	1610
X_c (mm), Antenna	0.04	0.05	0.05	0.01	0.01	0.01	0.01	0.01
X_c (mm), DFSICR	−0.01	0.00	0.00	0.00	0.01	0.13	0.20	0.32
Y_c (mm), Antenna	0.01	0.01	0.00	−0.01	−0.01	−0.01	−0.01	0.00
Y_c (mm), DFSICR	−0.01	0.00	−0.01	−0.02	−0.01	−0.01	0.00	0.01
Z_c (mm), Antenna	7.05	7.14	7.22	8.71	8.83	8.95	9.02	9.09
Z_c (mm), DFSICR	11.37	9.74	8.58	12.30	10.41	9.04	8.34	7.77

4.3.6 Prototyping

The design has been fabricated using three laminates of commercially available FR4 substrates (Shengyi S1000-2) with each laminate being 3.2mm thick. The folded corrugations are implemented by employment of metallized through-drilled walls and proper arrangement of copper cladding of substrates. The top view of top, middle, and bottom laminates as well as the assembled structure are shown in Fig. 4.15. Eight M3 Nylon screws are used to fasten the layers together. Additionally, since the performance of the structure is dependent on the electrical connection of the conductors and proper formation of the folded corrugations, the bottom of metallized drilled walls in each laminate are carefully soldered to the conductor layer of the laminate beneath it. Four strong clamps had been pressurizing the laminates during the soldering process to close any gaps between the laminates. Soldering is used to maintain the closed-gap state that the laminates experience under the pressure of clamps and ensure the proper electrical connection between metallic parts of folded corrugations. Finally, the electrical connections have been checked using a digital multimeter. It should be mentioned that the hole in the inner area of the DFSICR is designed to accommodate the feeding cable of the antenna being mounted on it.

Figure 4.15: Top view of the (a) Top laminate (b) Middle laminate (c) Bottom laminate (d) Assembled structure.

4.3.7 Measurement Results

The NovAtel GNSS-502 antenna has been mounted on the designed DFSICR and the radiation pattern of this configuration has been measured using the NSI anechoic near-field chamber at the University of Alberta. The measurement setup is shown in Fig. 4.16. The raw data is acquired in the cylindrical coordinate system with the source antenna sweeping a path along the vertical axis while the positioner rotates the antenna under test (AUT). Since the source antenna is linearly polarized, the magnitude and phase of the received signals are measured for two orthogonal polarizations, and are then combined using a computer code to obtain the RHCP and LHCP gains. The measured RHCP and LHCP gains of the structure are illustrated and compared with those of the simulations in Fig. 4.17 at the lower and upper edge of the operating frequency bands. One may observe that the measurement results are generally in good agreement with the simulations. There are small discrepancies between the simulated and measured radiation patterns which author believes might be a result of fabrication tolerances and near-field measurement imperfections. In spite of that, the structure demonstrates high polarization isolation at low-elevation angles as well as low back radiation. Polarization isolations of at least 15 dB over almost the entire upper hemisphere and measured front-to-back ratios of $20 - 25$ dB are achieved over both frequency bands. To better visualize the achieved polarization isolation, the measured ARs are depicted in Fig. 4.18. It can be seen that the ARs remains below 3dB from zenith to horizon over the upper frequency band. A close result is achieved over the lower frequency band with a slightly narrower 3-dB ARBW.

Also, the reflection coefficient (S_{11}) of the antenna has also been measured in presence and absence of the DFSICR. As Fig. 4.19 illustrates, the DFSICR does not affect the S_{11} of the antenna considerably.

In short, one can conclude that the required performance for multipath mitigating high-precision GNSS antennas has been met.

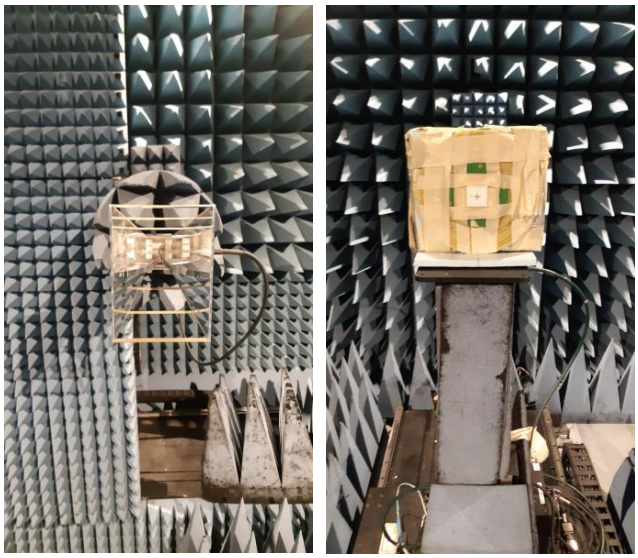

(a) (b)

Figure 4.16: Measurement setup (a) source antenna (b) antenna under test.

4.3.8 Comparison with Other Multipath Mitigating Ground Structures

In order to demonstrate the advantages of the proposed DFSICR, a comparison between the proposed configuration and other multipath mitigating ground structures is given in Table 4.2. In this comparison three EBG structures designed for GNSS applications are compared with the proposed DFSICR in addition to the conventional choke ring [7], and the dual-band dielectric-loaded choke ring reported in [8]. As one may observe, the EBG structures presented in [16] and [18] provide good front-to-back ratios and promising 3-dB ARBW with a relatively low height, however, they only cover one of the GNSS frequency bands. Besides, their lateral dimensions are about 30% larger than the DFSICR. The EBG structure introduced in [17], which is a modified version of [16], shows a dual-band behavior and a good front-to-back ratio, however, it suffers from very large area consumption due the larger size of its dual-band unit cell. Moreover, it shows a very narrow 3-dB ARBW. On the other hand, the dielectric-loaded choke ring reported in [8] demonstrates a generally better performance with smaller lateral dimensions compared to the aforementioned EBG structures. In spite of that, the height of the dielectric-loaded choke ring is still considerably high and the performance needs improvement over the lower frequency band. The DFSICR introduced in this work, however,

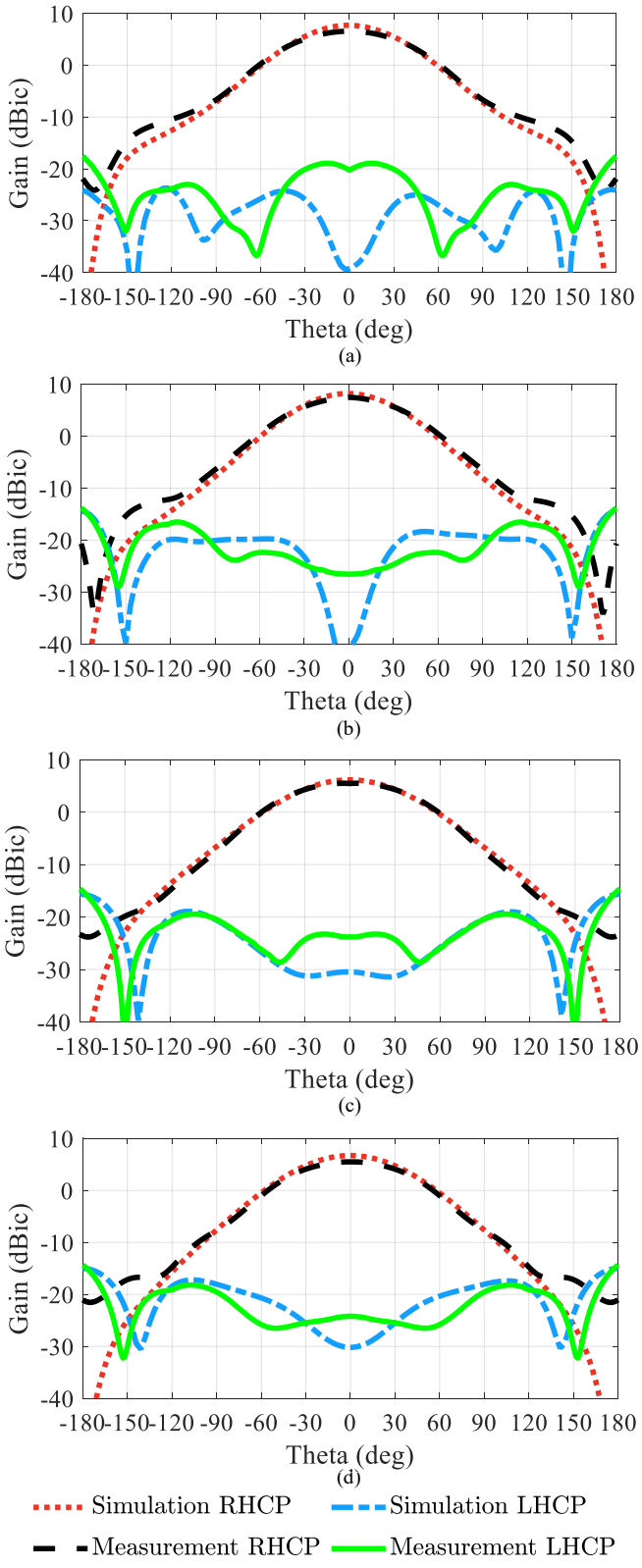

Figure 4.17: Comparison between the simulated and measured gains of the antenna mounted on DFSICR at (a) 1560 MHz (b) 1610 MHz (c) 1215 MHz (d) 1240 MHz.

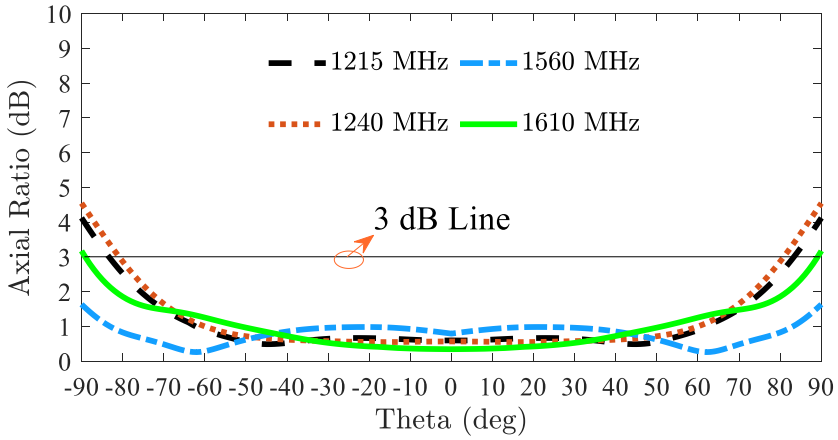

Figure 4.18: Measured ARs of the antenna mounted on DFSICR.

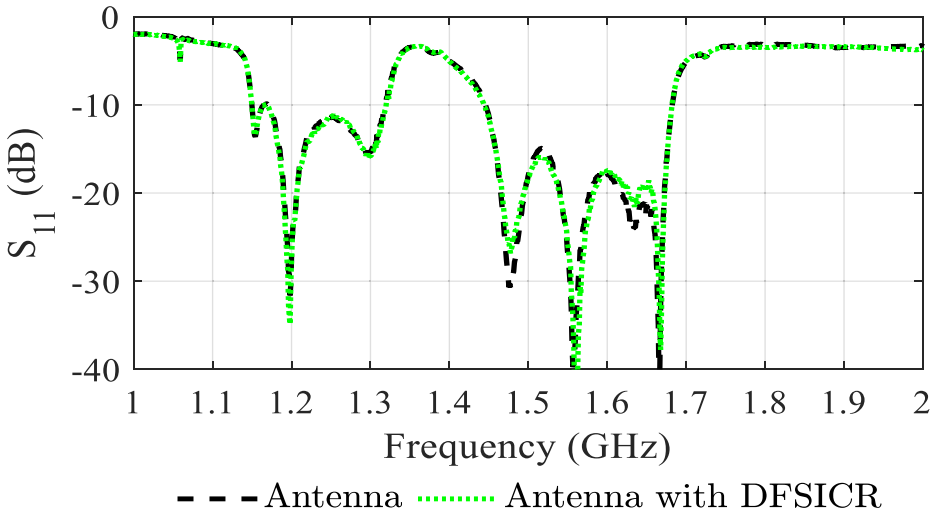

Figure 4.19: Measured S_{11} of the antenna with and without DFSICR.

outperforms the dielectric-loaded choke ring and demonstrates a very close performance to the conventional choke ring while it provides significant size and weight reduction. The DFSICR is 85% and 67% smaller in height compared to the classic choke ring and dielectric-loaded one, respectively. Also, the DFSICR shows size reductions of 38% and 20% in diameter with respect to the aforementioned designs. Moreover, it demonstrates weight reduction of more than 90% compared to the conventional choke rings. The weight of the DFSICR is less than 0.5 Kg whereas the weight of a classic choke ring structure is about 5 Kg. Thus, the proposed DFSICR demonstrates a great potential to be employed in multipath mitigating GNSS systems.

Table 4.2: Comparison between the proposed DFSICR and other multipath mitigating ground structures

Reference	Frequency Bands	Technology	Material
[16]	L1	EBG	Foam ($\epsilon_r = 1$)
[18]	L1	EBG	Not named ($\epsilon_r = 7$)
[17]	L1, L2	EBG	Foam ($\epsilon_r = 1$)
[7]	1.15-1.65 GHz	Choke Ring	Hollow corrugation ($\epsilon_r = 1$)
[8]	L1, L2	Choke Ring	FR4 ($\epsilon_r = 4.4$)
This work	L1, L2	DFSICR	FR4 ($\epsilon_r = 4.7$)

Reference	Max Lateral Size (mm)	Height (mm)	3-dB ARBW (degrees)	Front-to-back (dB)
[16]	300 (1.56λ)	10 (0.052λ)	140	22
[18]	286 (3.93λ)	7 (0.096λ)	170	20
[17]	428 (1.73λ)	10 (0.041λ)	$40 - 60$	$24 - 27$
[7]	360 (1.38λ)	66 (0.253λ)	$160 - 180$	$23 - 27$
[8]	280 (2.38λ)	29.2 (0.250λ)	$90 - 160$	$17 - 22$
This work	224 (1.97λ)	9.6 (0.085λ)	$160 - 180$	$20 - 25$

λ is the wavelength inside the dielectric material at the lowest frequency of operation.

Chapter 5

Conclusion and Future Directions

In this chapter the contribution of this work is summarized and the potential future research directions are presented.

5.1 Overall Contributions

In chapter 3 of this thesis, a novel technique for miniaturization of corrugated structures is presented and folded corrugations are introduced. The proposed folded corrugated structure is rigorously analyzed using the modal expansion method and equivalent circuit of a folded corrugation is derived using this analysis. It is demonstrated that the slit in a folded corrugation can be modeled with a capacitance. Analytical formulas for calculating the slit capacitance are derived and the effect of corrugation dimensions on the value of slit capacitance and consequently, corrugation resonance frequency are studied. The concept of folded corrugations is expanded to multi-folded corrugations and a time-efficient procedure for the design of multi-folded corrugated structures is presented using the extracted equivalent circuit and analytical formulas. Moreover, a design guide for realization of dual-band multi-folded corrugated structures is presented.

Three compact substrate integrated choke ring structures are designed and presented in chapter 4. In the first design, dual-band SICR, the via holes and copper cladding of substrates have been configured to realize two sub-

strate integrated corrugations with different depth and consequently, a dual-band HIS. Next, a folded-miniaturized SICR, FSICR, is designed using the proposed folded corrugations to obtain multipath mitigation over the upper GNSS frequency band. Finally, a low-profile dual-band double-folded SICR, DFSICR, is presented which brings about surface wave suppression and multipath mitigation over the L2, L1, and G1 GNSS frequency bands. All of the proposed designs demonstrate great multipath suppression characteristics, close to the classic choke rings, while they provide substantial reductions in height, diameter, and weight compared to the them.

5.2 Future Directions

Spoof surface plasmon polariton (spoof SPP) structures, also known as plasmonic materials, have been in great interest in the recent years. SPPs are highly localized surface waves that generally appear on the interface of two medium with opposite permittivities [33]. SPP modes naturally appear on the metal plates in the near infrared regime. Due to their high field confinement, SPP-enabled transmission lines, components, and devices are highly attractive for modern communication and sensing systems that require signal integrity, interference suppression, and compactness at the same time. Different textured structures have been proposed to imitate the surface plasmon behaviour in the microwave and terahertz frequencies among which corrugated structures have received great attention [33], [34]. Numerous passive and active components have been designed such as power dividers [34], directional couplers [34], frequency splitrers [35], resonators [36], filters [37], logic gates [38], and reconfigurable and programmable SPP transmission lines [38]. However, further miniaturization of these devices is required for low-frequency applications. The author believes that the folding miniaturization technique introduced in this work is promising to be applied to the present SPP components for further miniaturization.

References

[1] E. Kaplan and C. Hegarty, "Undestanding GPS/GNSS: Principles and applications," in *GNSS Technology and Applications series*, Artech House, 2017.

[2] M. Maqsood, S. Gao, T. Brown, and M. Unwin, "Effects of ground plane on the performance of multipath mitigating antennas for GNSS," in *2010 Loughborough Antennas & Propagation Conference*, 2010, pp. 241–244.

[3] C. J. Comp and P. Axelrad, "Adaptive SNR-based carrier phase multipath mitigation technique," *IEEE Transactions on Aerospace and Electronic Systems*, vol. 34, no. 1, pp. 264–276, 1998.

[4] L. Wanninger and M. May, "Carrier-phase multipath calibration of GPS reference stations," *Navigation*, vol. 48, no. 2, pp. 112–124, 2001.

[5] D. F. Betaille, P. A. Cross, and H.-J. Euler, "Assessment and improvement of the capabilities of a window correlator to model GPS multipath phase errors," *IEEE transactions on aerospace and electronic systems*, vol. 42, no. 2, pp. 705–717, 2006.

[6] Z. Zhang, B. Li, Y. Gao, and Y. Shen, "Real-time carrier phase multipath detection based on dual-frequency C/N0 data," *GPS Solutions*, vol. 23, no. 1, p. 7, 2019.

[7] F. Scire-Scappuzzo and S. N. Makarov, "A low-multipath wideband GPS antenna with cutoff or non-cutoff corrugated ground plane," *IEEE transactions on antennas and propagation*, vol. 57, no. 1, pp. 33–46, 2009.

[8] M. K. Emara, J. Hautcoeur, G. Panther, J. S. Wight, and S. Gupta, "Surface impedance engineered low-profile dual-band grooved-dielectric choke ring for GNSS applications," *IEEE Transactions on Antennas and Propagation*, vol. 67, no. 3, pp. 2008–2011, 2019.

[9] M. Emara, "Dispersion engineered radiative & guided-wave electromagnetic structures for efficient wave control," Ph.D. dissertation, 2018. DOI: 10.22215/etdsw/2018.2835.

[10] F. Khosravi, H. Moghadas, and P. Mousavi, "A GNSS antenna with a polarization selective surface for the mitigation of low-angle multipath interference," *IEEE Transactions on Antennas and Propagation*, vol. 63, no. 12, pp. 5287–5295, 2015.

[11] C. C. Counselman, "Multipath-rejecting GPS antennas," *Proceedings of the IEEE*, vol. 87, no. 1, pp. 86–91, 1999.

[12] J. R. Lambert, C. A. Balanis, and D. DeCarlo, "Spherical cap adaptive antennas for GPS," *IEEE Transactions on Antennas and Propagation*, vol. 57, no. 2, pp. 406–413, 2009.

[13] A. Rivera-Albino and C. A. Balanis, "Adaptive spherical array with non-uniformly spaced taps for GPS signal processing," in *2011 IEEE International Symposium on Antennas and Propagation (APSURSI)*, IEEE, 2011, pp. 2837–2840.

[14] M. M. Honari, R. Mirzavand, J. Melzer, and P. Mousavi, "A new aperture antenna using substrate integrated waveguide corrugated structures for 5G applications," *IEEE Antennas and Wireless Propagation Letters*, vol. 16, pp. 254–257, 2016.

[15] M. M. Honari, R. Mirzavand, and P. Mousavi, "A high-gain planar surface plasmon wave antenna based on substrate integrated waveguide technology with size reduction," *IEEE Transactions on Antennas and Propagation*, vol. 66, no. 5, pp. 2605–2609, 2018.

[16] R. Baggen, M. Martınez-Vázquez, J. Leiss, S. Holzwarth, L. S. Drioli, and P. de Maagt, "Low profile GALILEO antenna using EBG technology," *IEEE transactions on antennas and propagation*, vol. 56, no. 3, pp. 667–674, 2008.

[17] M. Maqsood, S. Gao, T. Brown, J. Xu, and J. Li, "Novel multipath mitigating ground planes for multiband global navigation satellite system antennas," in *2012 6th European conference on antennas and propagation (EUCAP)*, IEEE, 2012, pp. 1920–1924.

[18] H. R. Khaleel, H. Al-Rizzo, A. Isaac, and A. Bihnam, "Multipath mitigation in high precision GPS systems using artificial magnetic conductors," in *2014 IEEE Antennas and Propagation Society International Symposium (APSURSI)*, IEEE, 2014, pp. 432–433.

[19] D. Pozar, *Microwave Engineering*. Wiley, 2011, ISBN: 9780470631553.

[20] P.-S. Kildal, A. A. Kishk, and S. Maci, "Special issue on artificial magnetic conductors, soft/hard surfaces, and other complex surfaces," *IEEE Transactions on Antennas and Propagation*, vol. 53, no. 1, pp. 2–7, 2005.

[21] D. Sievenpiper, L. Zhang, R. F. Broas, N. G. Alexopolous, and E. Yablonovitch, "High-impedance electromagnetic surfaces with a forbidden frequency band," *IEEE Transactions on Microwave Theory and techniques*, vol. 47, no. 11, pp. 2059–2074, 1999.

[22] D. F. Sievenpiper, "High-impedance electromagnetic surfaces," Ph.D. dissertation, 1999.

[23] S. Arora, V. S. Puram, B. S. Reddy, V. S. kumar, C. Sriharsha, and D. V. Ramana, "X-band choked horn antenna for on-board TTC downlink of deep space satellite applications," in *2017 IEEE International Conference on Antenna Innovations & Modern Technologies for Ground, Aircraft and Satellite Applications (iAIM)*, 2017, pp. 1–5.

[24] S. S. Hesari and L. Knee, "Design and analysis of three Q-band feed horns for radio astronomy applications," in *2020 IEEE USNC-CNC-URSI North American Radio Science Meeting (Joint with AP-S Symposium)*, 2020, pp. 5–6.

[25] W. Nawaz and A. S. Ali, "Improvement of gain in dual fed X band isoflux choke horn antenna for use in LEO satellite mission," in *2015 Fourth International Conference on Aerospace Science and Engineering (ICASE)*, 2015, pp. 1–4.

[26] V. Akan, "Choke ring horn antenna design for satellite payload data transmitters," *Microwave and Optical Technology Letters*, vol. 63, no. 7, pp. 1913–1919, 2021.

[27] D. J. Sawyer, S. Das, N. Diamanti, A. Peter Annan, and A. K. Iyer, "Choke rings for pattern shaping of a GPR dipole antenna," *IEEE Transactions on Antennas and Propagation*, vol. 66, no. 12, pp. 6781–6790, 2018.

[28] C. Molero, R. Rodríguez-Berral, F. Mesa, and F. Medina, "Analytical circuit model for 1-D periodic T-shaped corrugated surfaces," *IEEE Transactions on Antennas and Propagation*, vol. 62, no. 2, pp. 794–803, 2014.

[29] R. Rodriguez-Berral, C. Molero, F. Medina, and F. Mesa, "Analytical wideband model for strip/slit gratings loaded with dielectric slabs," *IEEE Transactions on Microwave Theory and Techniques*, vol. 60, no. 12, pp. 3908–3918, 2012.

[30] *VEXXIS GNSS-500 series antennas*, `https://novatel.com/products/gps-gnss-antennas/vexxis-series-antennas/vexxis-gnss-500-series-antennas`, 2016.

[31] B. Akrour, R. Santerre, and A. Geiger, "Calibrating antenna phase centers," *GPS World*, pp. 49–53, 2005.

[32] J. M. Tranquilla and B. G. Colpitts, "GPS antenna design characteristics for high-precision applications," *Journal of Surveying Engineering*, vol. 115, no. 1, pp. 2–14, 1989.

[33] W. X. Tang, H. C. Zhang, H. F. Ma, W. X. Jiang, and T. J. Cui, "Concept, theory, design, and applications of spoof surface plasmon polaritons at microwave frequencies," *Advanced Optical Materials*, vol. 7, no. 1, 2019.

[34] D. Martın-Cano, M. Nesterov, A. Fernandez-Dominguez, F. Garcia-Vidal, L. Martin-Moreno, and E. Moreno, "Domino plasmons for subwavelength terahertz circuitry," *Optics Express*, vol. 18, no. 2, pp. 754–764, 2010.

[35] X. Gao, J. Hui Shi, X. Shen, H. Feng Ma, W. Xiang Jiang, L. Li, and T. Jun Cui, "Ultrathin dual-band surface plasmonic polariton waveguide and frequency splitter in microwave frequencies," *Applied Physics Letters*, vol. 102, no. 15, 2013.

[36] X. Shen and T. Jun Cui, "Planar plasmonic metamaterial on a thin film with nearly zero thickness," *Applied physics letters*, vol. 102, no. 21, 2013.

[37] X. Gao, L. Zhou, Z. Liao, H. F. Ma, and T. J. Cui, "An ultra-wideband surface plasmonic filter in microwave frequency," *Applied Physics Letters*, vol. 104, no. 19, 2014.

[38] H. C. Zhang, T. J. Cui, J. Xu, W. Tang, and J. F. Liu, "Real-time controls of designer surface plasmon polaritons using programmable plasmonic metamaterial," *Advanced Materials Technologies*, vol. 2, no. 1, 2017.